

## ABSTRACT

Title of thesis: FABRICATION OF ALL-THIN-FILM  
MAGNETO-ELECTRIC COUPLED MEMORY  
DEVICES

Arun Luykx, Master of Science, 2010

Dissertation directed by: Professor I. Takeuchi  
Department of Materials Science and Engineering

Spintronics are electronics based on manipulating the spin of electrons. Spintronics is currently commercially applied in the form of magnetic read heads in hard drives that use the giant magnetoresistive effect (GMR), and more recently the tunnel magnetoresistive effect (TMR). TMR, spin-valves, and spin torque transfer devices have generated interest towards the production of magnetic random access memory (MRAM devices). A major disadvantage of the current spin torque transfer approach to MRAM is that the magnetizing current needs to be substantial ( $10^{11}$  A/m<sup>2</sup> has been reported). In this research, we studied a novel approach to MRAM using magneto-electric coupled devices: heterostructures consisting of at least two materials, one piezoelectric, and the other magnetostrictive, that are connected by mechanical coupling. The principle of operation is that strain in one layer is transferred to another layer due to mechanical transduction, causing a change of properties in the layer onto which the strain is applied. In direct magneto-electric coupling, magnetostrictive strain due to the applied magnetic field is coupled to the piezoelectric layer with a voltage output as the result. The converse can also take place, where an applied voltage to the piezoelectric layer causes a strain change (converse piezoelectric effect) that is mechanically coupled to the magnetostrictive layer, changing its magnetic anisotropy (Villari effect). Our converse magneto-electric

heterostructure consists of mechanically coupled PZT (piezoelectric) and FeGa (magnetostrictive) thin films. The PZT layers, grown by sol-gel, acquire different strain states when an electric field is applied to them. Mechanical transduction couples this strain to the mechanically coupled FeGa layer (deposited by sputtering), which then changes its magnetic anisotropy. We can assign the change in magnetism to be two states, '0' and '1'. This thesis discusses the fabrication of a converse magneto-electric memory element that is non-volatile, low power consuming, and all-thin-film. By being non-volatile it shall retain its memory state, even after an external electric field has been removed. A low power and all thin film configuration allow this device to be potentially implemented on an integrated circuit scale.

FABRICATION OF ALL THIN FILM MAGNETO-ELECTRIC  
COUPLED MEMORY DEVICES

By

Arun Luykx

Thesis submitted to the Faculty of the Graduate School of the  
University of Maryland, College Park, in partial fulfillment of  
the requirements for the degree of  
Master of Science  
2010

Advisory Committee:

Professor I. Takeuchi (Chair, Advisor)

Professor J. Cumings

Professor L. Salamanca-Riba

© Copyright by

Arun Luykx

December, 2010

## Acknowledgements

I would like to start by expressing my appreciation to the thesis committee, Dr John Cumings and Dr Lourdes Salamanca-Riba, for reviewing my thesis and my defense, and for their input towards this work.

My sincerest thanks to my advisor, Dr Ichiro Takeuchi, for his guidance and support over the past three years. I particularly appreciated his understanding that, despite the fact gradstudents are used to a lot worse, he always put us up in good accommodations, and never made it that we had to worry about money for research. He provided me with a very good basis from which to do research.

My appreciation extends to my research group, for their film growing and analysing abilities, not to mention their quick turn around time and excellent conversations.

Had R.D. Vispute not hired me about five and a half years ago to work for him at the (then) Center for Superconductivity Research, I would have never considered graduate school, for which I thank him.

Of course, none of this would have been at all possible if not for my parents' support. No matter where we were on earth, they always fought for the best possible education for my siblings and myself (sometimes literally). Ever since I can remember they have always fully supported and encouraged my endeavours, from the time that I tried to sell an operating system (I myself wrote in Basic) to my neighbours, to my deciding to stop the plans of a Ph.D. I have always relied immensely on their support and guidance, and will never be able to thank them enough for what they have done for me. I should also apologise in advance for something my mother will certainly notice during the course of

this text: the incorrect usage of ‘z’ instead of ‘s’, and the letters ‘r’ and ‘e’ mixed up, which goes against all 12 years of British English education I’ve had.

I would like to thank my officemates, Paris Alexander, Dwight Hunter, Luz Sanchez, and Richard Suchoski for the pleasant times we had, and the welcome distractions from reading papers and analyzing data.

Very fruitful technical, but also often non-technical, conversations were had with Doug Bensen and Brian Straughn from CNAM, Jack Touart from the Physics Electronics Shop, and also John Abrahams, Jon Hummel, and Tom Loughran from the FabLab. One could argue the main reason I made it to campus as punctually and often as I did was because of their automotive advise over the years.

Many thanks to Sam Lofland for letting us use his FMR setup at Rowan University, and for his help in analysing the data.

My Nability and Raith skills would be non-existent today if not for the expertise training I received from Kamal Baloch, Todd Brintlinger, and Dan Lenski. I truly appreciate the many hours they spent sitting next to me.

On that note I should thank the Raith corporation for making my life a living hell for about a year, and then all the times they kept coming back to follow up.

Finally, I would like to thank my most significant contributor, Luz Sanchez, for her putting up with my often stressed out and erratic self, and most notably for putting up with my rather poor choice of cars. I have no idea where I would be today, Luz, if you weren’t by me all the times I came home frustrated and just feeling ‘done with everything’. Thank you for your undying companionship and patience during this, arguably one of the most difficult things I’ve ever done.

## Table of Contents

|   |    |
|---|----|
| Acknowledgements                          | ii |
| Table of Contents                         | iv |
| List of Figures                           | vi |
| Chapter 1: Motivation and Core Concepts   | 1  |
| Spintronics and The Future of Memory      | 1  |
| Piezoelectricity                          | 4  |
| Magnetostriction                          | 5  |
| Magneto-Electric Coupling                 | 7  |
| A Converse Magneto-Electric Memory Device | 9  |
| Multiferroics                             | 10 |
| Chapter 2: Sample Fabrication             | 12 |
| PZT                                       | 12 |
| PZT Bi-layers                             | 13 |
| FeGa                                      | 18 |
| Device Fabrication                        | 20 |
| Principle of Operation                    | 28 |
| Chapter 3: Characterization Methods       | 29 |
| FMR                                       | 29 |
| AMR                                       | 32 |
| Chapter 4: Results and Discussion         | 33 |

|  |    |
|--|----|
| FMR                                    | 33 |
| AMR                                    | 43 |
| Chapter 5: Conclusions and Future Work | 47 |
| Kerr Microscopy                        | 47 |
| SEMPA                                  | 50 |
| Conclusions                            | 52 |
| Appendix                               | 56 |
| Igor FMR processing code               | 56 |
| References                             | 61 |

## List of Figures

|  |    |
|--|----|
| Figure 1, A simplified spin-valve device with two different magnetization configurations.  | 2  |
| Figure 2, Spin-orbit coupling is what causes magnetostriction.   | 6  |
| Figure 3, A heterostructure (left) before and (right) after an electric field is applied to the medium. Note the strain change after a field has been applied.   | 7  |
| Figure 4, A direct magneto-electric coupled device. A voltage pulse is measured when the device is brought into a magnetic field due to the coupled magnetostrictive and piezoelectric effect.   | 8  |
| Figure 5, Schematic of a converse magneto-electric device with a top layer of variable resistance depending on the strain state of the piezoelectric film.   | 8  |
| Figure 6, Phase diagram of PZT (Source: 13)  | 13 |
| Figure 7, Cross-sectional TEM image of the PZT bilayers with (inset) close-up of the twin boundaries in the top layer.   | 14 |
| Figure 8, (Left) a-c ferro-elastic domains, (right) motion after applied electric field.   | 15 |
| Figure 9, Out-of-plane and in-plane PFM images of the PZT bi-layers before (left), and after -5 V (center) and +5 V (right) are applied in a 500x500 nm square. Note how the piezoresponse has changed in the areas where the voltage was applied. | 16 |
| Figure 10, Effective magnetostrictive constant as a function of gallium concentration in FeGa (Source: 17)   | 19 |
| Figure 11, Magnetization of FeGa as a function of magnetic field, and (inset) closeup of the hysteresis. (Source: 17)  | 20 |

|  |    |
|--|----|
| Figure 12, Cross-sectional SEM image of sputtered FeGa grown on PZT showing good FeGa/PZT interface.   | 20 |
| Figure 13, (left) Electron diffraction and (right) TEM image showing the polycrystalline nanograins of the FeGa film.  | 22 |
| Figure 14, (Top) first stage after all films have been deposited, (middle) second stage after the first milling session, (bottom) third stage after second milling, SiO <sub>2</sub> insulating layer is sputtered, and gold electrodes have been deposited.   | 23 |
| Figure 15, SEM image of four wire bonded electrodes on a SiO <sub>2</sub> /PZT arm of the cross, large FeGa area towards the bottom of the arm, gold electrodes, and (inset) close-up with dimensions of this FeGa device and gold electrodes. Author acknowledges the Nanocenter and MRSEC for equipment used to take this image. | 26 |
| Figure 16, A typical FMR setup. (Source: 22)   | 30 |
| Figure 17, An ideal derivative FMR signal.   | 32 |
| Figure 18, (Left) a typical AMR graph showing resistivity as a function of angle (source: 23), and (right) a typical AMR setup of a magnetic sample within an electromagnet at static field.   | 32 |
| Figure 19, Schematic of (left) top down and (right) side view of the FMR device.   | 36 |
| Figure 20, (Red) Original data, (Blue) processed data, (green) fitted FMR absorption plots.  | 40 |
| Figure 21, Formatted FMR data with (red circles) interesting x-axis cross over feature.  | 42 |
| Figure 22, Close-up of the 'flat' region on the FMR data over a +/-/+ voltage cycle.   | 43 |
| Figure 23, Change in magnetic anisotropy as a function of applied electric field. X-axis values are a representation of the pulse number.  | 44 |

|   |    |
|---|----|
| Figure 24, Our AMR setup with (inset) closeup of device in chip carrier.  | 46 |
| Figure 25, AMR measurements of the transport device under several bias schemes applied in order of top to bottom. Resistance on the y-axis, and in-plane rotation on the x-axis.  | 61 |
| Figure 26, Schematic of Kerr microscope (Source: 25)  | 62 |
| Figure 27, Image from a Kerr optical microscope showing magnetic domains on a 100nm FeGa thin film grown on Si, taken at 50x.   | 64 |
| Figure 28, A 50x50 mm FeGa/PZT device with a magnetic domain boxed in red, taken at 100x.   | 65 |
| Figure 29, Sempa images showing (clockwise from top left) film morphology, magnetization plot (with color disk showing magnetic field direction), vertically applied magnetic field, horizontally applied magnetic field. Note vertical magnetic domains. | 67 |
| Figure 30, MFM images (Top) as grown and (bottom) +7V applied for 30 seconds permalloy film on PZT bilayers, showing out-of-plane magnetic state change.  | 68 |

## Chapter 1

# Motivation and Core Concepts

## **Spintronics and the future of memory**

Today, when you go to a computer parts store, you have several choices in computer memory depending on your needs. Magnetic hard drives, and to a lesser extent magnetic tapes, are a reliable and very cheap, but relatively slow, method of storing and recalling information that is not needed right away. Flash memory in the form of USB memory sticks or other solid-state media is quickly becoming a viable alternative to magnetic media. The price per megabyte is still going down, albeit not as rapidly as the price per megabyte of magnetic media. Read times of solid-state devices are also considerably faster than conventional hard-drives. However, write times are, due to their technology, slower than a magnetic medium when it comes to large memory sizes. A recent report showed a sustained transfer rate of 110 MB per second for a conventional hard drive, and 56/32 MB per second (reading/writing, resp.) for a flash solid state device [1]. Random access memory in the form of DRAM or SRAM is a much faster way of accessing and writing data, but comes at a much higher cost and is volatile, as opposed to the other technologies mentioned above that are non-volatile (which retain their memory state even after an external power source has been removed).

Since the 1990s, a new field with promises of faster access times and cheaper memory has started developing. Spintronics, or spin electronics, is the study of manipulating the spin of an electron to make electronic devices. It is already commercially applied in the

form of read heads in magnetic hard drives that use the giant magnetoresistive effect (GMR), and more recently the tunnel magnetoresistive effect (TMR). The latter is an extension of GMR, which involves the concept of spin valves: two magnetic layers are separated from each other by a thin insulator. When the magnetic polarization directions of the two magnetic layers align, the device resistance is low. Conversely, if the polarization directions oppose, device resistance is high, as illustrated in figure 1. In this setup one magnetic layer is hard, and the other soft. It is the soft layer of the read head that changes its magnetic polarization from being in close proximity to the magnetic medium which it is reading. This then causes an overall a high or low device resistance, due to its spin valve properties, which is then assigned to be a '0' or '1' state.

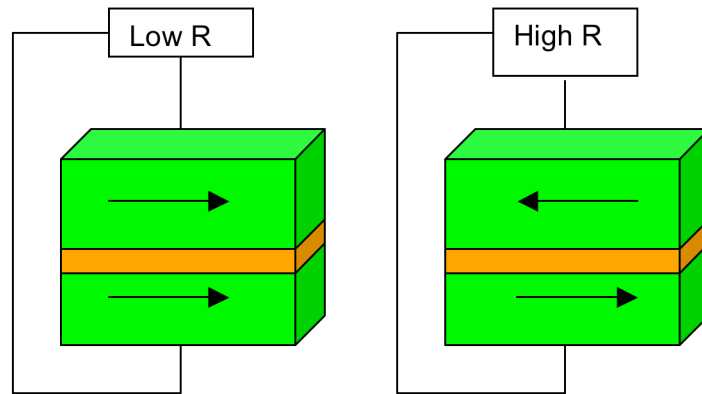


*Figure 1, A simplified spin-valve device with two different magnetization configurations.*

More recently, TMR and spin-valves have generated interest towards the production of MRAM, or magnetoresistive random access memory, devices. Instead of using the technology to read magnetic media in the read head of a magnetic hard drive, here the magnetization of the soft layer is the actual memory bit. Reading is still done by measuring the overall resistance, but the change in magnetization is done by applying a directional current in a wire over the soft layer. The current induces magnetization in the

top layer, causing it to change its magnetic polarization. This is known as spin torque transfer. As such, magnetization can be changed from one state to another, creating a '0' and '1' situation. The major disadvantage of this technique, and reason it has still not been implemented on a wide scale, is that the magnetizing current needs to be substantial ( $10^{11}$  A/m<sup>2</sup> has been reported [2]), which is not useful in low power applications.

In this research we studied a novel approach to MRAM. More specifically, we studied the feasibility of using a combination of a piezoelectric layer and a magnetostrictive layer to make a new form of spintronic memory device. Our device is to be non-volatile, low power, and all thin film. Since non-volatile, it can retain its memory state, even after external power has been removed. A low power and all thin film setup allows this device to be implemented on an integrated circuit scale.

Magneto-electric coupled devices are heterostructures consisting of at least two materials, one piezoelectric, and the other magnetostrictive, that are connected by mechanical coupling. The principle of operation is that strain in one layer is transferred to another layer, due to mechanical transduction, causing a change in its properties. In direct magneto-electric coupling, magnetostrictive strain, due to the immersion into a magnetic field, is coupled to the piezoelectric layer with a voltage output as the result. The converse is also true, where an applied voltage to the piezoelectric layer causes a strain change in itself, but also the mechanically coupled magnetostrictive layer, changing its magnetic anisotropy. This is discussed in more detail in a following section.

We have developed a converse magneto-electric memory element. The key materials on our memory device are iron-gallium (FeGa) and lead-zirconate-titanate ( $\text{Pb}(\text{Zr},\text{Ti})\text{O}_3$  or PZT). FeGa is a known magnetostrictive material, and PZT is a widely studied and industrialized piezoelectric material. Making a heterostructure of FeGa and PZT allows us to change the magnetic anisotropy of FeGa by using the Villari effect, with strain induced by an applied electric field to the mechanically coupled PZT layer underneath. By combining their magnetostrictive and piezoelectric properties we are able to demonstrate a novel all thin film converse magnetoelectric and multiferroic memory device. Details follow in the following sections and chapters.

## **Piezoelectricity**

The piezoelectric effect is the dielectric polarization of a material due to an applied mechanical strain to the system [25]. The converse piezoelectric effect is the opposite, where an electric field applied to the material causes a mechanical strain.

This is due to certain materials having an inversion symmetry breaking crystal structure. When strain is applied to such a system, the asymmetrical positive and negative charges are no longer in their initial state, and a dipole moment is created. Conversely, when an electric field is applied to the system, the charges change location depending on the applied field, causing a physical expansion or contraction of the material.

The piezoelectric effect is described mathematically by a modified version of Hooke's law and :

$$D = \epsilon E + dS$$

$$T = cS - dE$$

Where  $D$  = electric flux density,  $\epsilon$  = dielectric permittivity,  $E$  = electric field strength,  $d$  = piezoelectric constant,  $S$  = strain, and  $T$  = stress. Note that  $d$ , the piezoelectric constant, is a tensor. This is to reflect a different effect depending on the direction of polarization, illustrated by a subscript of two numbers;  $d_{ab}$ . The x,y, and z axis are represented by 1,2, and 3, respectively. Shear around these axis are 4, 5, and 6 respectively. In our work, as we are working with thin films, we are most interested in the  $d_{33}$  (out-of-plane strain when an out-of-plane applied electric field is applied) and  $d_{31}$  constants (in-plane strain due to an out-of-plane applied electric field).

## **Magnetostriction**

A major part of this technology revolves around the concept of magnetostriction. The observation of this effect is similar to piezoelectricity, in that an applied *magnetic* field causes a physical change in the film, causing it to deform. The actual mechanics of the operation, however, are very different to piezoelectricity.

The concept of magnetostriction arises from the electron spin-orbit coupling within a magnetostrictive material. Figure 2 (top) illustrates the initial condition, on which we see randomly oriented spins. After a magnetic field has been applied (figure 2, bottom) we see how the spins align, creating an additional length  $\Delta L$ .

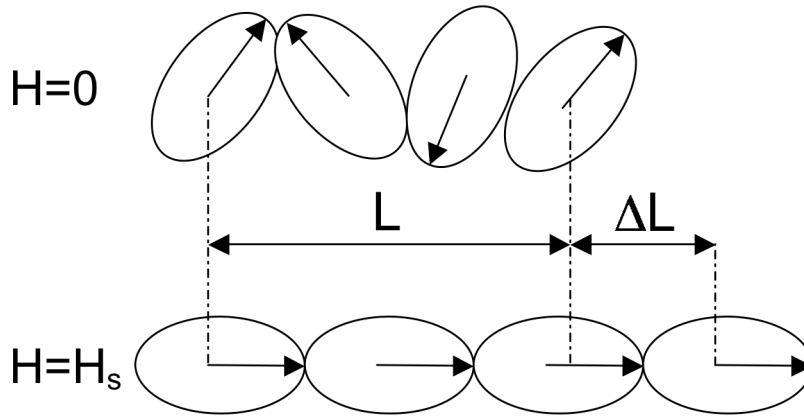


Figure 2, Spin-orbit coupling is what causes magnetostriction.

This change in  $L$  is used to characterize the magnetostrictive constant,  $\lambda$ :

$$\lambda = \frac{\Delta L}{L}$$

The larger  $\lambda$ , the larger the deformation after a field is applied. Therefore it is usually beneficial to have materials with a large magnetostrictive constant.

In our device we will be applying strain to the magnetostrictive film causing it to change its magnetic anisotropy. This is the Villari effect, or the reverse of the magnetostrictive effect. The strain, due to reversible twin boundary motion in the ferroelastic layer, is from an applied electric field to a piezoelectric material onto which the magnetostrictive film is in mechanical contact. Figure 3 illustrates what happens; more details on this are provided in the next section.

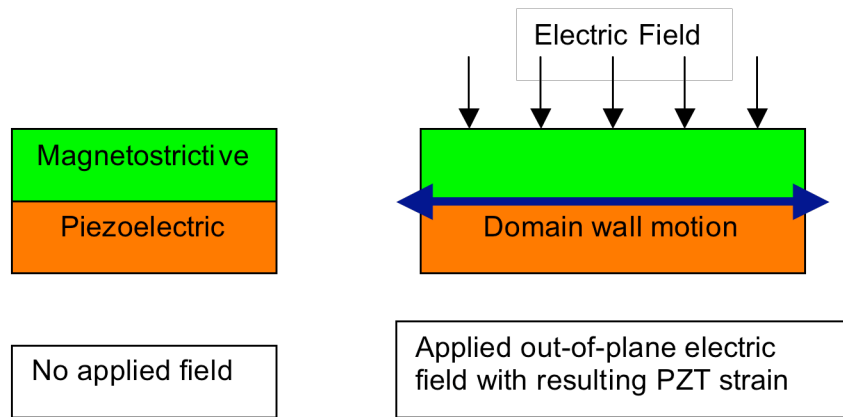


*Figure 3, A heterostructure (left) before and (right) after an electric field is applied to the medium. Note the strain change after a field has been applied.*

## **Magneto-Electric Coupling**

We will focus primarily on magneto-electric coupling as the result of physical contact of two materials, and mechanical transduction at the interface.

Magneto-electric coupling is the combination of piezoelectric and a magnetostrictive material, that together make a heterostructure. When the combination is put under certain conditions, such as when an electric or magnetic field, the strain state of one layer changes. This is due to either the magnetostrictive or the converse-piezoelectric effect, depending on the type of applied field. Because the two layers are mechanically coupled together, mechanical transduction imposes this change in strain on the other layer, causing it too to change its internal properties. This change can then be measured. There are two types of magneto-electro coupling: direct and converse coupling.

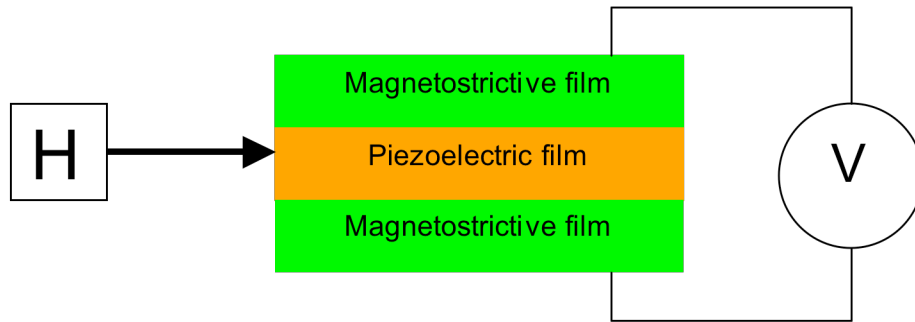


*Figure 4, A direct magneto-electric coupled device. A voltage pulse is measured when the device is brought into a magnetic field due to the coupled magnetostrictive and piezoelectric effect.*

In direct magneto-electric coupling the heterostructure is used to achieve an electric response to an imposed magnetic field. The sample, illustrated above (figure 4) as a piezoelectric sandwiched between two magnetostrictive layers, is placed in a magnetic field. Due to the properties of the magnetostrictive layer, a strain change occurs in these layers when magnetic field is applied. Because the layers are mechanically coupled together, the strain change is also imposed on the piezoelectric layer, causing a change in its polarity due to the  $d_{31}$  piezoelectric effect. This can be measured as an electric field. A potential application for this technique is a highly sensitive magnetometer, as is currently being investigated by Zhao et al [6].

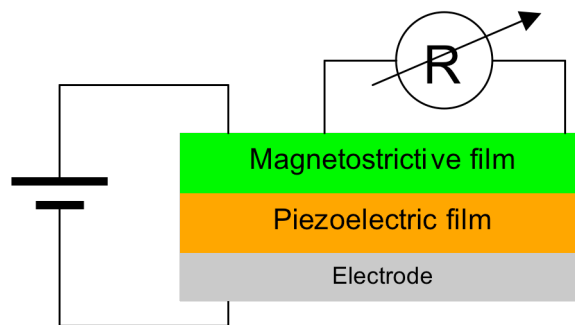


*Figure 5, A converse magneto-electric device with a top layer of variable resistance depending on the strain state of the piezoelectric film.*

The opposite of this is the converse magneto-electric effect, where the magnetic anisotropy of the magnetostrictive layer is changed (Villari effect) due to a strain change caused by the piezoelectric layer (piezoelectric effect) as a result of an applied voltage [19]. Figure 5 illustrates this. This change in magnetic anisotropy can then be measured, for example, by measuring the magnetoresistance. Potential applications for this are magnetic memory devices.

This thesis focused primarily on the converse magneto-electric effect, and its implementation as a demonstration of an all-thin-film magnetic memory device. The converse ME effect has been previously demonstrated by Overby et al [7] as a combination of a GaMnAs thin film and a bulk PZT sample. Our device will be a combination of two thin films: iron-gallium (FeGa) and lead-zirconium-titanate ( $\text{Pb}(\text{Zr},\text{Ti})\text{O}_3$ ).

## **A Converse, Magneto-Electric Memory Device**

Our goal was to demonstrate that a combination of a piezoelectric and magnetostrictive thin film is a viable implementation of converse magneto-electric coupling as a magnetic memory element. This device will have the following properties:

- Non-volatile
  - Non-volatile memory is memory that can retain its state even after an external power source has been removed. Current standard computer RAM is volatile, where its state is lost after the power has been shut down. Solid state drives are non-volatile, and do not lose their memory state after power has been

removed. Currently volatile memory has faster access times, and is therefore preferable as random access memory.

- Entirely made of thin films
  - Bulk materials have severe limitations in implementation in Si-based integrated circuits.
- Operation at room temperature
  - Room temperature operation allows for many more possibilities in consumer electronics.
- Operation at low fields and currents
  - To work in portable devices without severely impacting performance, battery life, and implementation, and to enable a high level of sensitivity.
  - Spin torque transfer (STT) is a competing technology. With this approach spin polarized current is used to electrically change the magnetization of a magnetic layer in a tunnel magnetoresistance (TMR) heterostructure. However, to generate spin polarized current, a large current density is needed (on the order of  $10^{11}$  A/m<sup>2</sup> [2]), which is not conducive towards low-power electronics. This is a limiting factor that is currently the source of much research.

## **Multiferroics**

Multiferroics are a group of materials that possess both ferroelectric and ferromagnetic properties. Thereby it is possible to take advantage of one material system with both properties for ME coupling, rather than combining two as we are doing with our work.

Examples of multiferroic materials are bismuth-ferrite ( $\text{BiFeO}_3$  or BFO), holmium-manganite ( $\text{HoMnO}_3$ ), terbium-manganite ( $\text{TbMnO}_3$ ), etc.

These materials are intrinsic multiferroics, in that magnetism and ferroelectricity co-exist naturally as bulk properties, and exhibit coupling effects [8]. However, magneto-electric coupling effects of these intrinsic materials are usually very small, and occur only at cryogenic temperatures or require large external fields (for example, magnetic fields in the range of teslas).

In our study we use a composite multiferroic system. Here, magneto-electric coupling is due to mechanical transduction from two coupled materials, with large effects at room temperature and without the application of large external fields.

## Chapter 2

### Sample Fabrication

The choice of materials is key to an effective converse magneto-electric effect. For our purposes we have chosen PZT (lead-zirconium-titanate,  $\text{PbZr}_x\text{Ti}_{1-x}\text{O}_3$ ) as our piezoelectric, and FeGa (iron-gallium) as the magnetostrictive layer. The following is a brief introductory discussion of their properties.

#### **PZT**

One major advantage to using PZT is that it has been studied for sixty years, and a significant amount of papers have been published on the material. The first paper on PZT was published in 1951 by Shirane et al [9]. Since then PZT has been used for a wide variety of applications, such as actuators, capacitors, and transducers. This is in part due to its ferroelectric and piezoelectric properties, its large dielectric constant [10], a morphotropic phase boundary near  $x=0.52$  (illustrated on figure 6), but also because of its flexibility in growth techniques. For thin film growth it has been successfully grown by PLD, sputtering, and sol-gel (11,12,10). For our purposes PZT will be spun by the sol-gel technique.

It is our goal to make all thin film devices. This means that every layer of the structure must be a thin film, instead of a combination of a bulk material and a thin film (as has been shown previously by Overby [7]). However, the main reason the technique of combining two materials to create magneto-electric coupling, where mechanical

transduction takes place at the continuous interface between the two layers, had not yet been attempted for thin films is due to the clamping effect: the strain state changes in the films are prevented by the substrate they are grown on. Due to the significant thickness difference between the substrate (~0.5mm) and the films (~150nm), the substrate is solid enough to overcome any attempt by the thin film to change strain state: it clamps the film down. In order for us to proceed, this needs to be overcome. This is where the solution of the PZT bi-layers comes in to play.

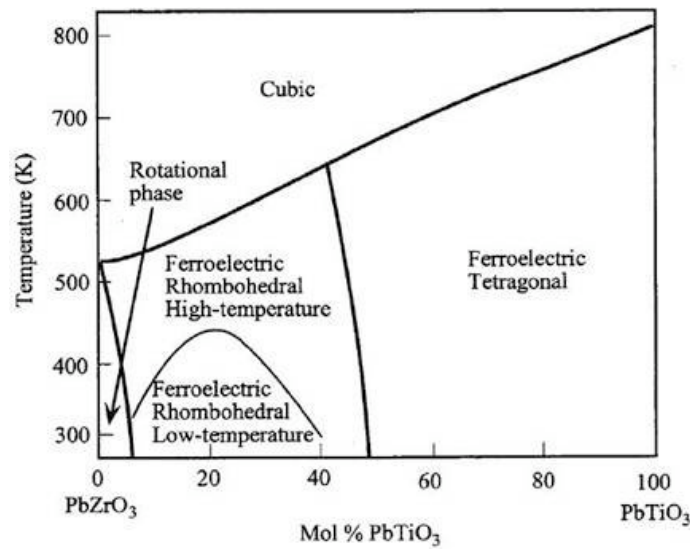


Figure 6, Phase diagram of PZT with varying concentration of Zr and Ti (Source: 13)

## PZT Bi-layers

The concept of the PZT bi-layers was pioneered by Kartawidjaja et al [14], and first implemented by Varatharajan et al [15].

From figure 6 we see how by varying the concentrations of Zr and Ti in the PZT solution we can attain different crystal structures. A 30%-70% concentration of Ti to Zr yields a rhombohedral crystal structure, whereas the opposite concentration is tetragonal.

Combining two films, one 30-70 and the other 70-30, we create a bi-layer of PZT with a rhombohedral configuration on the bottom, and a tetragonal configuration on the top [15]. Typical film thicknesses are 70 nm, each. Figure 7 shows a cross-sectional TEM image with the layers visible. Note the presence of a Pt/Ti layer, used as a bottom electrode for our experiments, which can be seen at the bottom of the structure.

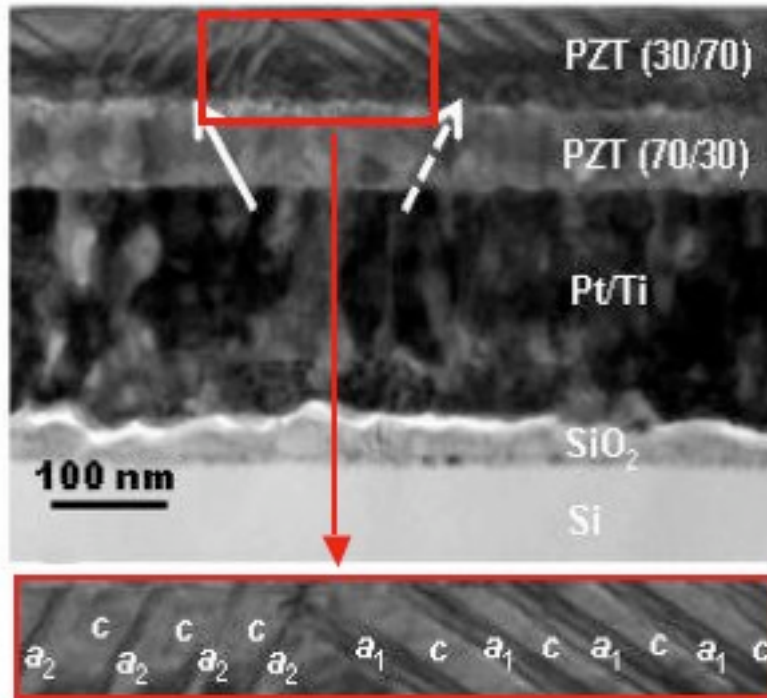


*Figure 7, Cross-sectional TEM image of the PZT bilayers with (inset) close-up of the twin boundaries in the top layer.*

Both these layers are piezoelectric, but act in different ways. When the top Zr rich PZT layer -with a/c 90 degree domain boundaries that move reversibly- changes strain state due to an applied electric field, the bottom PZT layer accommodates this strain change and allows it to change shape, thereby overcoming the clamping effect of the substrate. This is due to its rhombohedral crystallographic structure, which is partly labile.

The top layer, due to the presence of the a/c domains, keeps the strain state it attained

with the applied electric field until a reverse field is applied, at which point the twin boundary moves again. The close-up of the top of figure 7 shows an enlarged view of the top layer, on which you can see these twin-boundaries, and the ‘a’ and ‘c’ domains. The ‘a’ and ‘c’ domains are the in-plane and out-of-plane components, respectively. The cross-sectional TEM image in Figure 7 shows a c/a/c/a structure with (001)/(100) orientation (taken from Varatharajan et al, [15]). When an electric field is applied the domains flip, as illustrated in figure 8, thereby moving the domain wall. On a macroscopic scale this results in a strain change. The domains cannot flip back on their own, and so this domain wall movement is only reversed when an opposing field is applied.

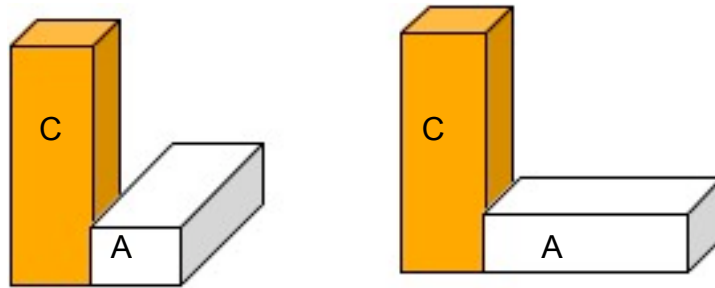


*Figure 8, (Left) a-c ferro-elastic domains, (right) motion after applied electric field.*

Varatharajan et al have extensively studied this bi-layer approach, and have performed measurements confirming its operation (found in the reference). The most compelling example of operation is displayed here with one of our PZT bi-layers. It is a piezo-force microscopy<sup>1</sup> (PFM) image in the virgin state, and after applying voltage biases to certain areas (figure 9). This PZT, on average, has a 1-2  $\mu\text{m}$  grain size.

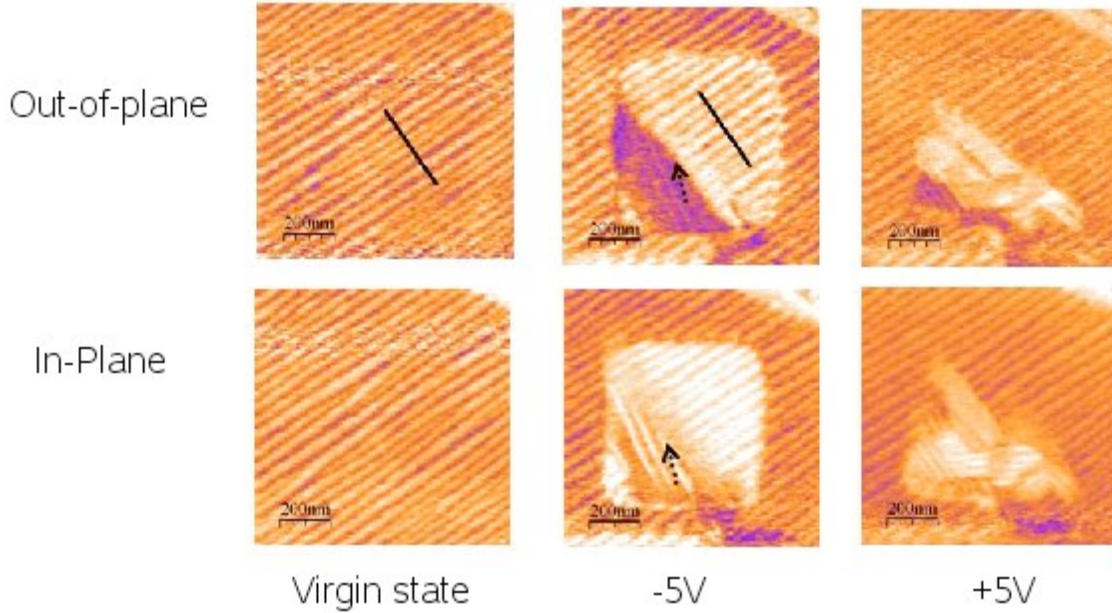


*Figure 9, Out-of-plane and in-plane PFM images of the PZT bi-layers before (left), and after -5 V (center) and +5 V (right) are applied in a 500x500 nm square. Note how the piezoresponse has changed in the areas where the voltage was applied.*

The AFM tip used for this PFM measurement was a Pt/Ir coated cantilever (7nm tip radius, 0.2N/m force constant, 13kHz resonant frequency). To obtain the in-plane and out-of-plane images, a 1.5V AC signal at 7 kHz was applied between the tip and the bottom electrode of the device. Two lock-in amplifiers were used to analyze the signal.

Figure 9 shows a PFM scan of a virgin 1x1  $\mu\text{m}$  area on the PZT bi-layers. With the tip operated in contact mode, a 500x500nm area is scanned. During this scan a voltage is applied to the tip, to polarize a PZT region. No measurements are taken at this stage, the scan is only to polarize areas of the film. The tip voltage is -5V, after which the voltage is

---

<sup>1</sup> Piezo-force microscopy: An add-on to an atomic force microscope (AFM), used in contact mode. PFM relays information on the piezoelectric response of a film. This is done by applying an alternating voltage to the probe tip, measuring the deformation on the surface (due to the converse piezoelectric effect) using the AFM's photodiode, and comparing the two signals using a lock-in amplifier. Both in-plane and out-of-plane response can be measured using this technique.

removed and a regular PFM scan of the area is performed. From figure 9 (center) we see how the ferroelastic domains have switched, though not uniformly. The tip voltage is then set at +5 V and the 500x500nm area is poled again. Figure 9 (right) shows the results, from which we again see how the ferroelastic domains have switched. From these images we can see how the in- and out-of-plane piezo-response has indeed changed as a function of the applied electric field. The PFM images of figure 9 show how the clamping effect has been overcome, and the PZT thin film bi-layers can indeed change their strain state irrespective of the substrate. Furthermore, it shows how these states do not revert back to a neutral position even after the electric field has been removed; they are non-volatile. However, it is apparent that not all domains switch the same way, or even back to their initial configuration.

In our case, PZT was deposited by sol-gel, following Kartawidjaja's recipe (with some modifications mentioned in 'Device Fabrication') [14]. Each PZT layer is 70nm, making a total of 140nm. The 50nm Pt bottom electrode, with 3nm Ti adhesive layer, were magnetron sputtered.

With the addition of a mechanically coupled magnetostrictive layer on top of the PZT bi-layers, in our case FeGa, we now have a magneto-electrically coupled device. We can now change the strain state of a PZT thin film, therefore we can now also change the magnetic anisotropy of the coupled magnetostrictive layer from one state to another, and back, as often as we want. The next section details FeGa, our choice of magnetostrictive material.

## FeGa

When choosing the magnetostrictive layer several requirements must be met. The material must have:

- A large magnetostriction constant ( $\lambda_{\text{eff}}$ )
  - The larger the magnetostrictive constant, the larger the Villari effect.
- A low coercive field
  - For a state switch to occur at lower magnetic fields.
- High magnetic permeability

In addition to this it is necessary for the material to retain its magnetostrictive properties as a thin film. Low or room temperature growth parameters are an additional advantage.

FeGa possesses many of these properties. During his studies, Hattrick-Simpers et al [17] published a combinatorial study of various concentrations of co-sputtered  $\text{Fe}_{1-x}\text{Ga}_x$  (with  $0 < x < 0.3$ ). In his study he found the  $\text{Fe}_{0.7}\text{Ga}_{0.3}$  thin film to have an effective magnetostrictive coefficient of around 140ppm. Recent studies by Hunter et al have shown that this number can be increased significantly by quenching [18]. This thesis, however, focuses on the growth technique used in the Hattrick-Simpers paper. Figure 10 shows the magnetostrictive constant as a function of gallium content using his growth technique. We will be using the  $\text{Fe}_{0.7}\text{Ga}_{0.3}$  composition (which henceforth will be referred to as FeGa). The large effective magnetostriction constant and low temperature growth parameters makes FeGa an ideal candidate for our ME-device.

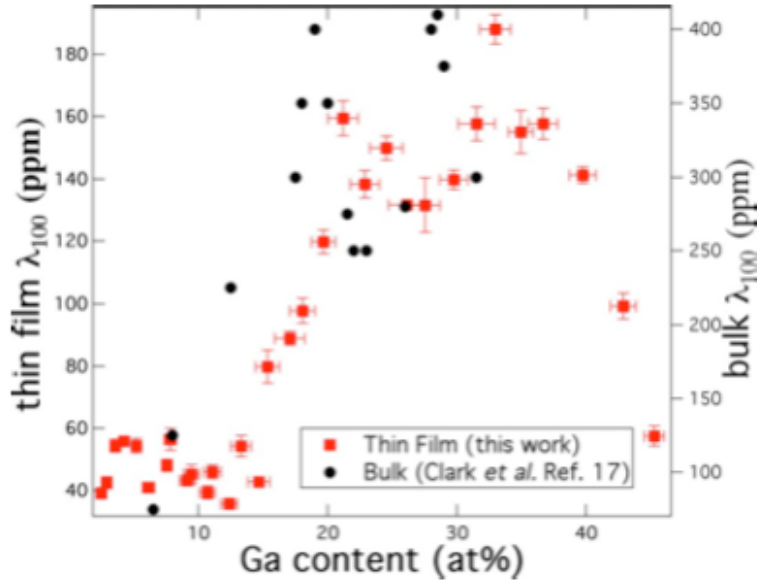


Figure 10, Effective magnetostrictive constant as a function of gallium concentration in FeGa (Source: 17)

Figure 11 shows the magnetic properties of FeGa: a coercive field at around 90 Oe (inset) and a saturation field of around 2000 Oe. With the goal of a memory device in mind, the low coercive field is ideal to show a distinct difference in magnetic state. The magnetic permeability of FeGa is  $290\mu_0$  [20].

FeGa is sputtered onto our PZT bilayers. AC magnetron sputtering at 120 W was used (details on fabrication in the next section). The interface between FeGa and PZT, as shown in the cross-sectional SEM image in figure 12, shows good contact. This is necessary for good mechanical transduction when FeGa is to be strained by the PZT layers.

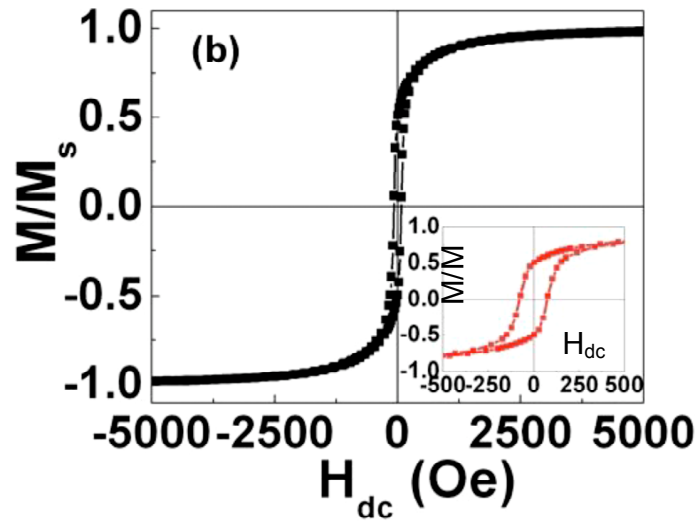


Figure 11, Magnetization of FeGa as a function of magnetic field, and (inset) close-up of the hysteresis. (Source: 17)

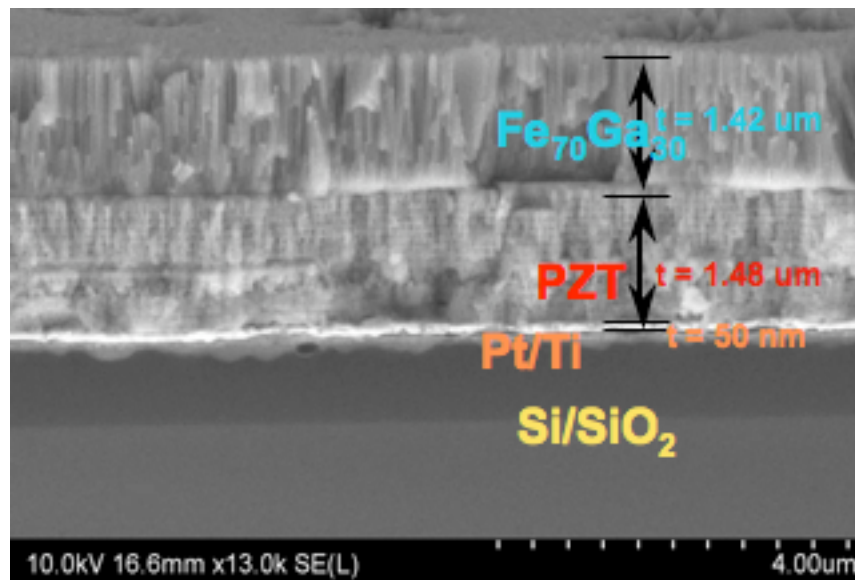


Figure 12, Cross-sectional SEM image of sputtered FeGa grown on PZT showing good FeGa/PZT interface.

With FeGa as our magnetostrictive material, and PZT as our piezoelectric, we now have a set of materials for our converse magneto-electric device.

## Device Fabrication

Polycrystalline platinum is sputtered onto a Si (100) wafer. This is the bottom electrode of the device.

The PZT films are grown by sol-gel onto the wafer. The two layers are 70 nm each. First the 70/30 (Zr-Ti) concentration is deposited, followed by the 30/70 concentration. In doing this the labile rhombohedral 70/30 is on the bottom in contact with the platinum. The top, 30/70, layer is tetragonal.

Both layers are deposited in an identical fashion, except for the precursor. Details on their production are described by Kartawidjaja et al [14]. The PZT pre-cursor with 10 mol% excess lead (no acetic acid) was spin-coated at 3000 rpm for 30 seconds, followed by 5 minutes of rapid thermal annealing at 500C. The sample is then placed on a hotplate at 300 C, then 500 C for 7 minutes. Finally, the sample is baked in a tube-furnace for an hour at 700 C in flowing oxygen. We typically also confirmed, by PFM, that the bi-layers were working as expected.

Finally, a 50nm FeGa film is magnetron sputtered with a 3nm Ti adhesive layer: 60W, 14.2 mm target-substrate separation, 4.6 mTorr Ar partial pressure, initial vacuum better than  $5 \times 10^{-8}$  Torr. The advantage of this technique is that large wafers can be coated at relatively low temperatures, with high quality films. In our equipment, wafers up to 4 inches can be processed. Electron diffraction results (figure 13, left) and TEM images (figure 13, right) show the film's consistency of polycrystalline nanograins. These grains

are essential for proper operation of our strain-induced magneto-electric coupled devices.

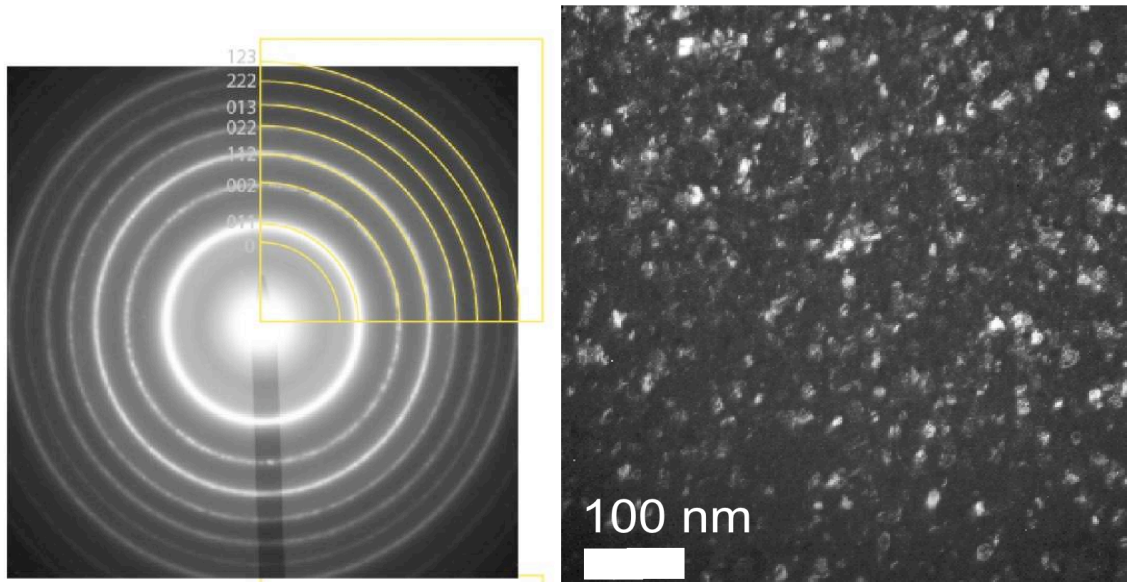
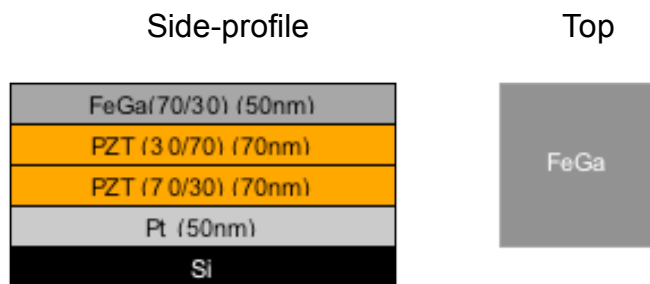
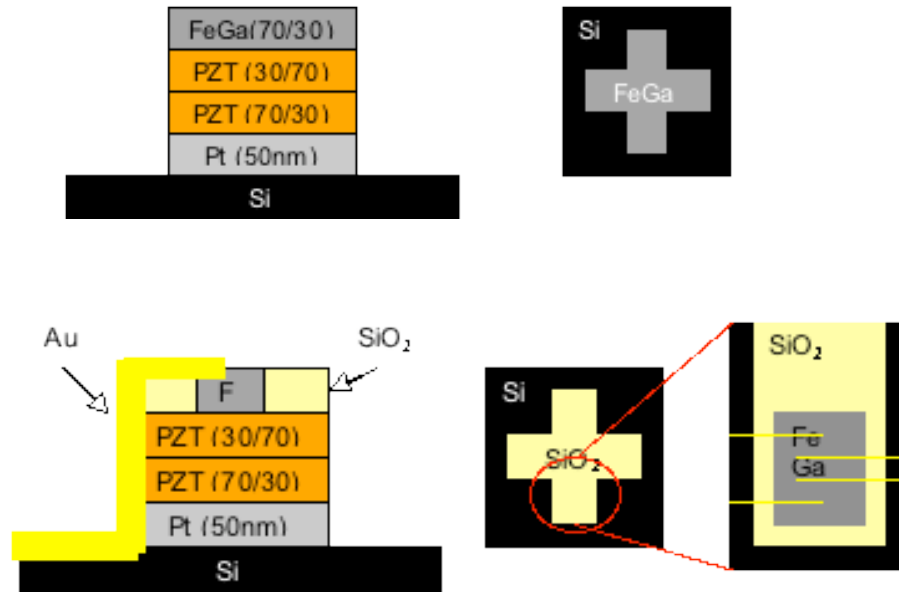


Figure 13, (left) Electron diffraction and (right) TEM image showing the polycrystalline nanograins of the FeGa film.

The top image on figure 14, below, is a cartoon of the wafer after all films have been deposited.





*Figure 14, (Top) first stage after all films have been deposited, (middle) second stage after the first milling session, (bottom) third stage after second milling, SiO<sub>2</sub> insulating layer is sputtered, and gold electrodes have been deposited.*

From here a cross is patterned onto the wafer with 1813 photoresist. The arms of the cross are 1.5 mm wide. The resist is spun on at 4000 rpm for 40 seconds, followed by 2 minutes on a hot plate at 95C. UV exposure time is 11 seconds, and finally a 20 second submersion into CD-26 developer.

After this all layers are ion-milled right through till the SiO<sub>2</sub>, leaving behind only a cross containing all layers (figure 14, middle). This is to allow for an area of bare, insulating SiO<sub>2</sub> onto which Au wires can be wirebonded. The chip can also be held safely in this area. The ion mill is a Commonwealth Scientific system, operated at 200W and 1 A neutralizer current,  $4 \times 10^{-4}$  Torr Ar partial pressure, better than  $8 \times 10^{-7}$  Torr base pressure, with a water-cooled stage and chamber jacket, and sample rotation of about 3 rotations per minute.

The photoresist from the previous step is stripped using acetone for approximately 30 minutes. The chip is then washed in isopropanol, and dried with N<sub>2</sub>. 1813 photoresist is applied again to pattern small squares on top of the cross (8 total, sizes varying from 5x5 μm to 50x50 μm). For certain experiments it was necessary to make a hall bar. To accomplish this a double exposure was used with the square mask, to create bars as small as 3x10 μm (photolithography tool stage control was a limiting factor for us). For this stage CD-30 developer is preferred, and only for 10 seconds, as it is better for developing small features (<20 μm).

The final ion-milling stage only mills through the top FeGa layer, leaving behind small FeGa square pads on top of a PZT bi-layer cross. In a final stage we make gold electrodes, which –due to their relatively large surface area- can short through the PZT layers. Therefore SiO<sub>2</sub> is typically deposited, by magnetron sputtering (300 W), before the gold electrode stage to create an extra insulation barrier. SiO<sub>s</sub> thickness is 0.7 times the thickness of FeGa. This is to accommodate for any lift-off spikes that might break continuity of the gold electrodes.

Again the photoresist is stripped, the sample is washed in isopropanol, and dried with nitrogen.

Gold contacts are then patterned onto this device by means of e-beam lithography. The lithography tool is a Nability system attached to a Philips XL-30 operated at 30 kV. The

resist comprises two layers: a bottom layer of MMA (4500 rpm for 50 seconds, bake for 7 minutes at 150 C,  $\sim 1.5 \mu\text{m}$ ), and a top layer of PMMA950 (6000 rpm for 50 seconds, bake for 7 minutes at 150 C,  $\sim 100 \text{ nm}$ ). Feature line-widths went from  $\sim 500 \text{ nm}$  and up, depending on the device size. The smallest features were written at  $110 \mu\text{C}/\text{cm}^2$ ; dosages for larger feature sizes were automatically calculated by the software.

By means of thermal evaporation we deposit around 150 nm-200 nm of gold. 20 minutes in acetone, followed by a washing in isopropanol, is typically sufficient to lift off the excess gold. Sonic-bathing is best avoided to preserve the tiny gold contacts on the surface of FeGa.

The bottom of figure 14 shows all deposited layers. Figure 15 is an example (with dimensions in the inset) of a completed hall-bar type device.

With our FeGa film sputtered on top of our PZT bi-layers we now have a combination of a magnetostrictive and a ferroelectric material. After all layers have been deposited and a gold contact has been added to the top, we have a device that looks like the scanning electron microscope (SEM) image in figure 15. The inset shows a close-up of the actual device on one arm of the cross, with gold contacts patterned by e-beam lithography. The bottom electrode is accessed by means of a wirebond to a large area of FeGa (approximately  $0.5 \times 0.3 \text{ mm}$ ), which shorts out through all layers to the bottom Pt layer.

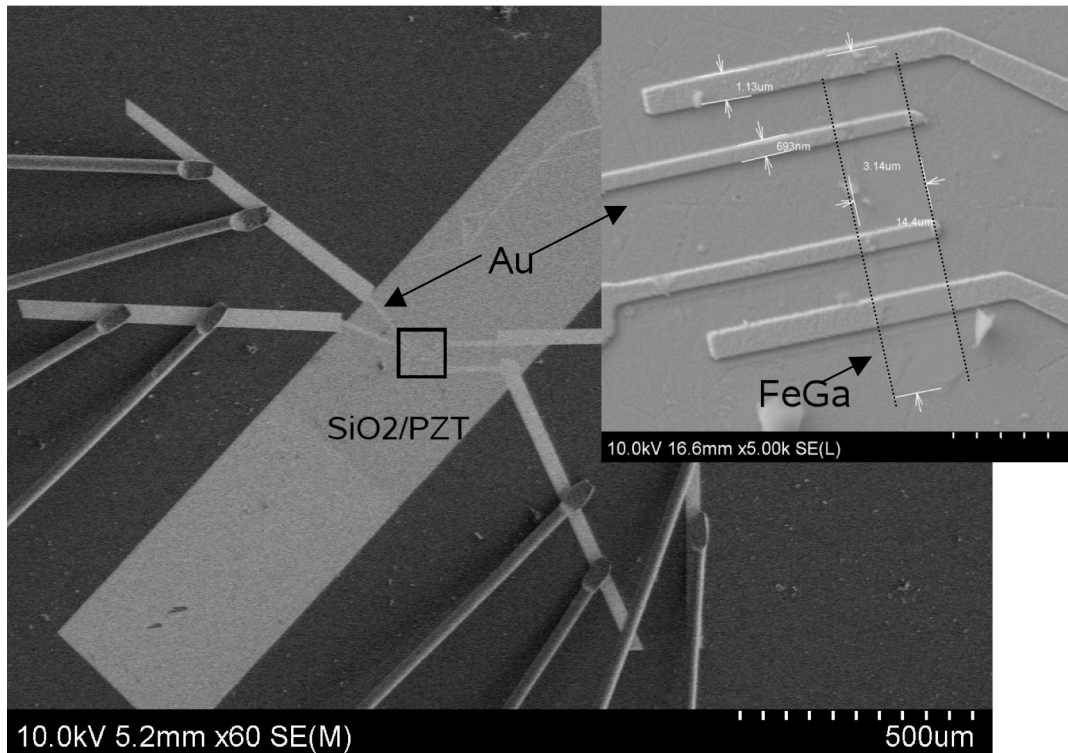


Figure 15, SEM image of four wire bonded electrodes on a  $\text{SiO}_2/\text{PZT}$  arm of the cross, large FeGa area towards the bottom of the arm, gold electrodes, and (inset) close-up with dimensions of this FeGa device and gold electrodes. Author acknowledges the Nanocenter and MRSEC for equipment used to take this image.

Some comments on fabrication:

- It is imperative all steps be done in a cleanroom facility whenever possible.
- To prevent FeGa from deteriorating, temperatures should never exceed 100 C. This causes gallium to oxidize and evaporate, and the FeGa film loses its magnetostrictive properties.
- When gold is deposited the stage should be tilted to improve gold continuity over the edges of the cross and the FeGa square pad.  $\text{SiO}_2$  lift-off spikes could further hamper continuity in these areas.
- Due to the two independent photolithography stages, it is not uncommon to make last minute e-beam pattern changes. Therefore we found a Nability system ideal for

our e-beam lithography needs. Its flexibility of use and (in our case) lower powered electron microscope made it very easy to find a device, observe its features from a large magnification, and write an on-the-fly pattern to it (based on a standard pattern; typically some features just needed to be moved a bit). Similar attempts were made using a Raith E-line system, but after many months of technical issues due to complications with the software and hardware interface, this was aborted.

- The quality of the PZT films are an essential component to the sandwich: the PZT must operate as required, but also be a strong dielectric. Should the PZT be leaky, the electric field would short out, and the entire device will not do anything. It is recommended that a PZT solution not be used past a month after initial production.
- The bottom Pt electrode must be polycrystalline for effective switching. Attempts at using textured Pt bottom electrodes yielded non-functioning PZT bi-layers.
- Any large conducting area will short out the PZT bi-layers. This includes FeGa, therefore its presence is usually limited to small pads, ranging from  $10 \times 3 \mu\text{m}$  to  $50 \times 50 \mu\text{m}$ . Gold is also kept to a minimum with small wires (700nm width) spanning the required surfaces. These wires enlarge to around 1 mm when off the PZT, at which point they are on the  $\text{SiO}_2$  surface and wire-bonded to a chip carrier.
- Wires smaller than 500nm were attempted, and successfully lifted off (as small as 250 nm). Unfortunately the effort required to make these wires serves little purpose, as devices commonly failed due to contacts blowing up.

- This author did not deposit any FeGa or PZT films himself but relied immensely on the help of his colleagues Dwight Hunter, Peng Zhao, and Matthias Wambach (FeGa), and Luz Sanchez and Fransiska Kartawidjaja (PZT).

## **Principle of Operation**

The principle of operation is relatively straightforward, and follows the converse-magneto-electric effect as described in the introduction: a voltage is applied to a gold electrode on top of the layers, with a large FeGa area shorting out to the platinum bottom electrode connected to the ground pin. In doing so the electric field is applied to both layers from top to bottom.

Due to this applied electric field the twin boundaries in the top PZT layer move, and the layer changes its strain state. Mechanical transduction transfers this strain to the FeGa layer, causing it to change its magnetic anisotropy (as a result of inverse magnetostrictive). Once the electric field is removed, the system retains its strain state due to the twin-boundaries in the top, tetragonal PZT layer. This means that the ‘new’ magnetic anisotropy in the FeGa is also preserved. The change in magnetic anisotropy can be measured using a four-probe measurement to measure its magnetoresistance. There two resistance values can be used to represent ‘0’ and ‘1’ states, which can be switched and measured using the electrodes already present. In effect, this is a readable and writeable bit of memory.

## Chapter 3

### Characterization Methods

Several techniques were used to study the properties of our ME device. This chapter will cover ferromagnetic resonance measurements (FMR), and anisotropic magnetoresistance measurements (AMR). This chapter will detail the characterization experiments, and discuss the results.

#### **FMR**

One use of probing ferromagnetic resonance is to characterize the change in magnetic anisotropy of a film. It shows the frequency absorption properties of a material due to spin precession, allowing the user to find a peak absorption frequency. This is known as the ferromagnetic resonance frequency, and is a defining characteristic of a magnetic material. We sweep the electromagnet and find a point of maximum absorption; this corresponds to a certain magnetic field intensity. Showing how this field of maximum absorption changes, reversibly, demonstrates that the magnetic anisotropy of the FeGa layer is indeed changing based on the strain state of the mechanically coupled PZT layers. This shows how we can change magnetic properties of a material with an applied electric field.

The sample is placed in a resonance cavity within the poles of an electromagnet. In this case, the magnet is swept over  $|0.5|$  T. A microwave source at the front of the cavity generates a 9 GHz frequency, the power intensity of which is detected at the end of the cavity by a detector diode. The effect of the electron spin precession frequency (based on

the magnetic field) on the cavity frequency results in a decrease of power (absorption). When the precession frequency equals the microwave source frequency we have a maximum power absorption. This happens at a corresponding magnetic field from the electromagnet. Figure 16 illustrates a typical FMR setup (source: 22).

The detector measures the change of the power through the cavity, so it should be noted that the observed reading is the derivative of the absorption. However, since we are primarily interested in the peak absorption frequencies, one only need note the zero-crossing of the x-axis. Figure 17 is an example graph of the output from a FMR setup.

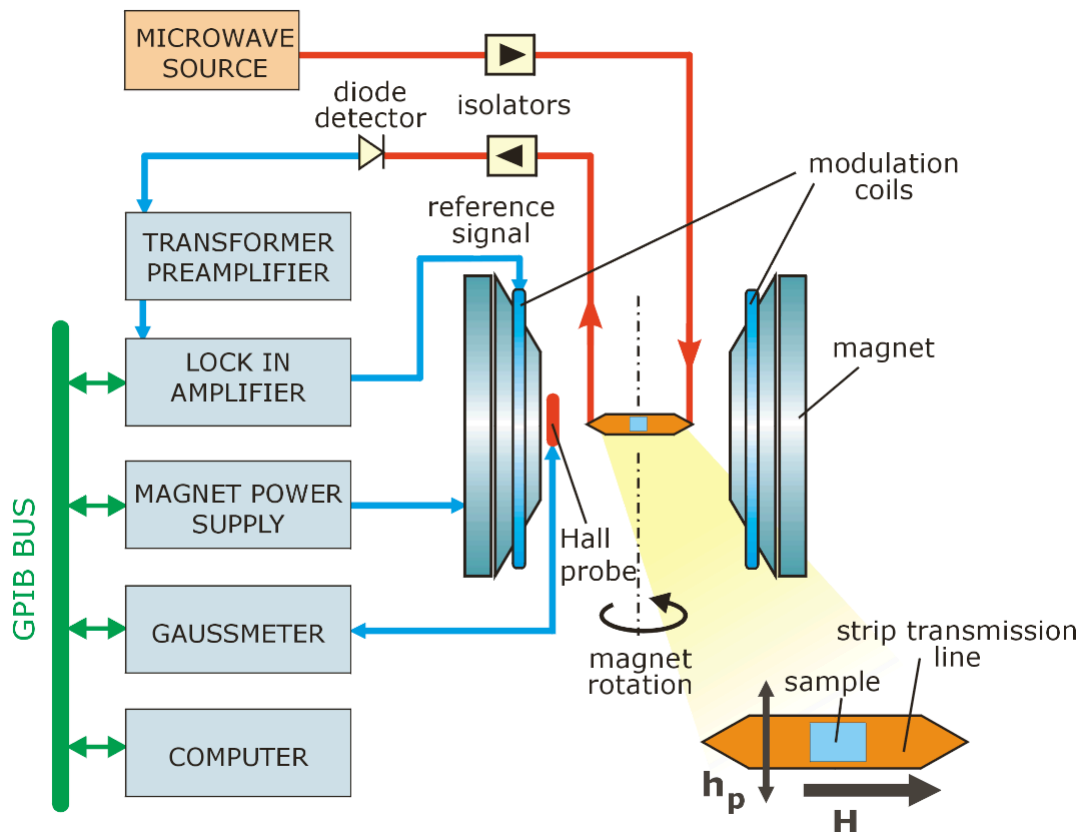


Figure 16, A typical FMR setup. (Source: 22)

The equation for the resonance frequency,  $\omega$  is given by [21]:

$$\omega = \gamma \sqrt{B_0(H + 4\pi M)}$$

Where  $\gamma$  = the gyro-magnetic ratio for an electron spin,  $M$  = the magnetization in the material, and  $H$  = the strength of the magnetic field. We are interested in the change in  $H$  ( $\Delta H$ ).

An ideal FMR signal is illustrated in figure 17. Imagine this being our device. From it one finds a maximum absorption (zero field crossing) at around 950 Oe, in the case of the example (this is  $H$  in the above equation). After applying an electric field causing a change of the strain in the PZT layers, and so also in the FeGa layer, we now have a ‘new’ state of magnetic anisotropy in the FeGa layer. This will be reflected by a change in the field at which peak absorption occurs, say for example it is now at 850 Oe. By applying an electric field with opposite sign we expect to go back to the original magnetic anisotropy, and so again have a peak absorption at 950 Oe. Like this we expect to be able to switch back and forth, showing that we are indeed able to change magnetic anisotropy by applying an electric field to the system.

The sample was rotated in-plane about 180 degrees, measurements taken at 10 degree intervals, to note possible differences due to uniaxial anisotropy. Results and discussion are found in the next chapter.

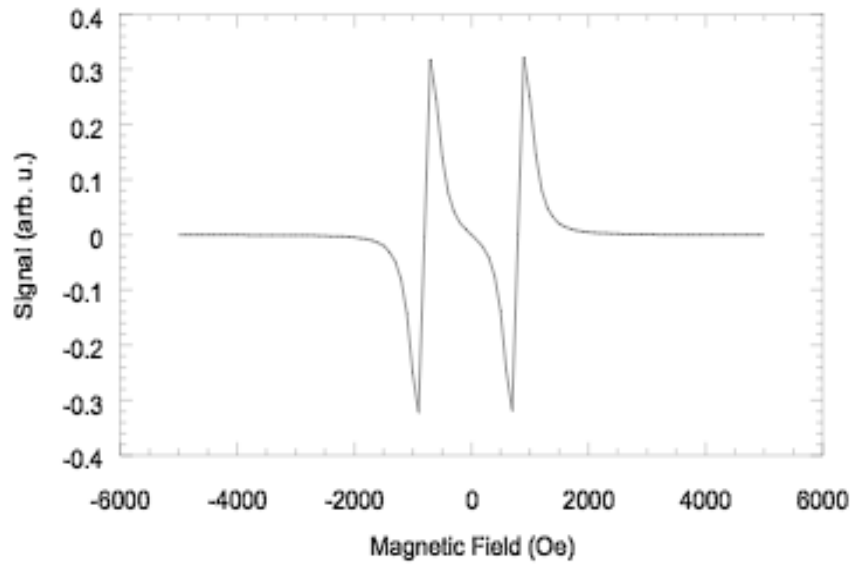


Figure 17, An ideal derivative FMR .

### Anisotropic Magnetoresistance

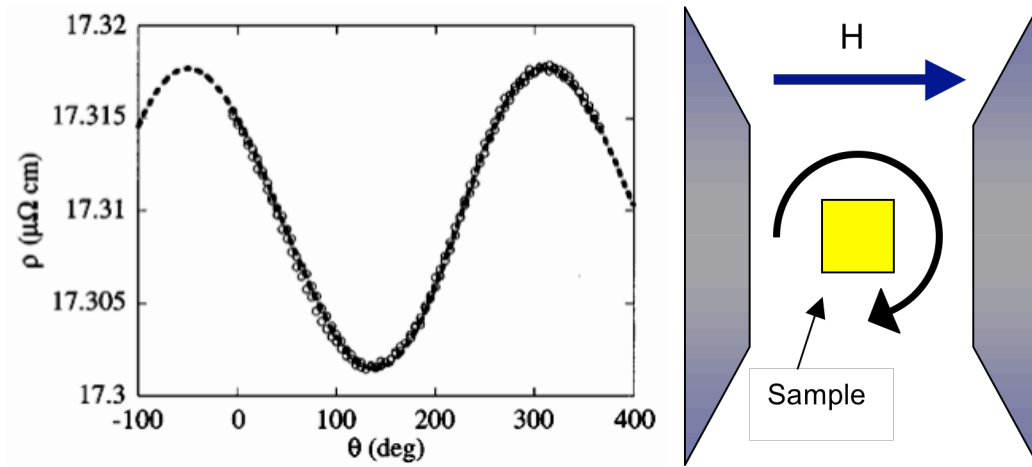


Figure 18, (Left) a typical AMR graph showing resistivity of Co/CoO bi-layer thin-films as a function of angle (source: 23), and (right) a typical AMR setup of a magnetic sample within an electromagnet at static field.

Anisotropic Magnetoresistance (AMR) is the study of the change in resistance of a magnetic material as a function of its position within a magnetic field. It is an in-plane or

out-of-plane, angular dependent measurement, where the four-probe resistance of the material (divided by its average resistance) is plotted as function of a corresponding angle within the field. In our case we are interested in the in-plane effects. AMR shows the change in resistance as magnetization changes from being perpendicular to parallel with the current. Resistance changes in the material due to electron scattering patterns differing based on the direction of the magnetic field. An electronic compass is an example of a direct use of anisotropic magnetoresistance.

The sample is placed in-plane within the poles of the electromagnet kept at 300 Oe. At this field FeGa is at saturation. The sample is in a structure that allows it to be rotated, in-plane, by 360 degrees. Four probe resistance measurements are taken every 7.5 degrees, and plotted. Figure 7 shows a typical result (left) and a cartoon of the setup (right).

Because we are changing the magnetic anisotropy of our FeGa film by applying an electric field to the system, we expect to see a shift in angle at which the maximum and minimum resistance values occur, as a function of the applied electric field. This shift should reverse when an opposing pulse is applied. By repeating this we will see, for a given value, differing resistance values corresponding to 0 and 1 states.

Four probe measurements are taken for better accuracy. Current is driven between two outlying contacts on the surface of our device, with voltage being measured on the center two contacts.

A common expression for AMR is:

$$AMR = \frac{\rho_{//} - \rho_{\perp}}{\rho_{avg}}$$

with, following Tondra et al [23],

$$\rho_{avg} = \frac{1}{3}\rho_{//} + \frac{2}{3}\rho_{\perp}$$

where  $\rho$  is resistivity.

## Chapter 4

# Results and Discussion

## **FMR**

### Setup

The details of ferromagnetic resonance measurements are discussed in the previous chapter. The advantage of this technique is that it is a relatively quick method of probing magnetic anisotropy, thereby verifying that our heterostructure does indeed present converse magneto-electric coupling. An FMR device has a relatively simple structure. This made it much more feasible to start with than transport measurements, which require substantially more complicated devices (as described in chapter 2). The immediate availability of equipment was an additional advantage.

FMR measurements probe the magnetic anisotropy of our FeGa film, and reveal the resonance absorption plot. From it we can find the peak absorption field (the zero magnetic field crossover;  $H$ ). After changing the magnetic anisotropy of FeGa (Villari effect) by changing the strain of the PZT layers with an applied electric field (converse piezoelectric effect), we expect to find a change in the peak absorption field ( $\Delta H$ ). Reversing the polarity of the applied electric field we expect to see a different peak absorption field. Repeating this several times shows a repeatable change in the peak absorption field.

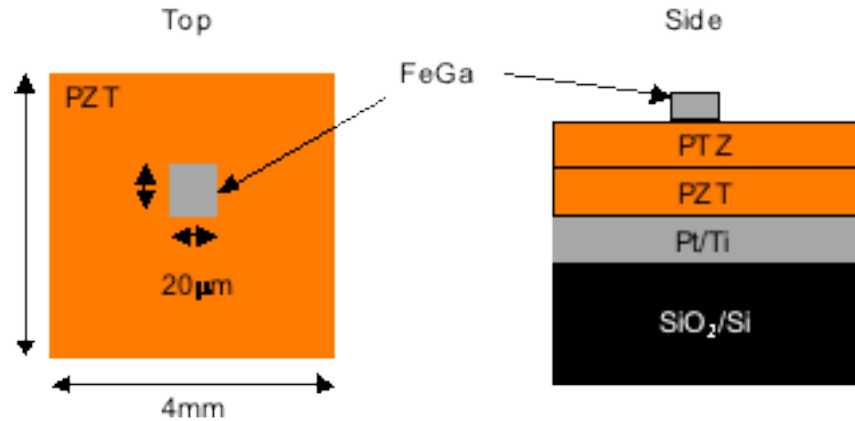


Figure 19, Schematic of (left) top down and (right) side view of the FMR device.

The basis for our FMR device was the standard PZT bi-layer setup, as described in chapter 2: Each PZT layer is 70 nm, with  $\text{PbZr}_{0.3}\text{Ti}_{0.7}\text{O}_3$  on top and  $\text{PbZr}_{0.7}\text{Ti}_{0.3}\text{O}_3$  on the bottom. The bottom electrode is 50 nm Pt, with a 3nm Ti adhesive layer. The actual FMR device was a single 20x20 µm 50 nm thick FeGa pad, patterned on the surface of the PZT bi-layers, by means of photolithography using the standard 1813 settings described in chapter 2. The entire chip was around 4x4 mm. Figure 19 is a cartoon showing the layout of the device. It was placed in-plane within the magnets, and was turned by 180 degrees, with measurements taken every 10 degrees.

Due to the complex nature of the PZT domain switching, it is very important that our FeGa pad be small, on the order of a micron. Like this it is less likely a pad will cover multiple grains, as the strain effects in neighbouring PZT grains could cancel each other out, reducing the change in magnetic anisotropy of the FeGa layer. Figure 9 shows how ferroelastic domain switching is not entirely uniform. Ideally, an FeGa pad fits on top of one of the 1-2 µm PZT grains to cover a larger area of uniformly switched ferroelastic

domains. Unfortunately a device of those dimensions would be too small for FMR measurements, as the effects are then too small to measure. Our choice of device size, 20x20  $\mu\text{m}$ , was large enough to show different resonant frequencies, but small enough to show the effects of strain.

### Experimental

Our device was as pictured in figure 19. It should be noted that only one 20x20  $\mu\text{m}$  device was present on the entire 4x4 mm surface. Using a probe station, a conducting probe tip was brought to the FeGa pad. This probe was connected to a wire for macroscopic use. Part of the PZT was scratched away using a diamond scribe to reveal the bottom electrode. Using a multimeter to measure resistance from that scratch to another one made on a different part of the chip, a low resistance ( $\sim 0.3$  ohms) confirmed it as the bottom electrode. Next, using the probe station, the resistance of the FeGa pad and the bottom electrode was measured. This was infinite, and confirmed the FeGa device had not shorted through the PZT. This infinite resistance is necessary to apply an electric field to the device from the FeGa pad through the PZT to the bottom electrode.

The device was placed in the cavity of the FMR setup between the poles of the electromagnet, noting the orientation of the chip (for future replacement), such that the film structure was in-plane with the magnetic field. The magnetic field is swept from -0.5 T to 0.5 T, monitored by a magnetometer. The microwave source operates at 9 GHz. The detector diode is interfaced with a computer, on to which the derivative of the absorption is plotted. Measurement sweeps are taken at the initial position inside the cavity, and then

again every 10 degrees till the sample is rotated 180 degrees in-plane. With this we have a data set of 18 plots representing the magnetic anisotropy of the device in its virgin state. The device is removed from the cavity and placed on the probe station. There the positive output pin on an HP DC power supply was attached to the probe tip, and the negative output pin to the scratch on the bottom electrode. A 3V pulse is applied by turning the power supply on for a moment, then off again. In doing this we have applied an electric field to the heterostructure. This field causes the piezoelectric PZT to move its domain boundaries, causing a strain state change. The magnetic anisotropy of the mechanically coupled FeGa layer changes because of this strain change (Villari effect). Finally, when the voltage is removed, the anisotropy is retained due to the twin boundary motion of the PZT layer, which will only move when a reverse voltage is applied. This is state '1'

Note that as this device is non-volatile, the voltage is only momentarily applied (about 10 seconds).

We replace the chip exactly in the cavity as before (we previously noted the orientation for this reason). Again, 18 measurements are taken at 10 degree intervals under the same conditions as the previous set.

The sample is removed and placed in the probe station. A -3 voltage is applied to the device, causing a different strain state and so a different magnetic anisotropy. We will call this state '0'. The chip is replaced in the cavity, and the same measurements are taken.

This was repeated several times, for several devices. An additional FMR measurement was taken before a new device was placed without anything in the cavity (other than the standard holder) as a background measurement run.

Although 18 measurements were taken at 10 degree intervals, the only difference between them was a magnetic hysteresis of changing magnitude depending on the rotation. The angle with the largest magnetic hysteresis was used for all data sets (specific angle not mentioned here because the initial in-plane placement of the sample is random).

### Modelling

Once the data sets were collected it was necessary to fit them to a model so the sets could be correlated. From these sets we extracted the resonance absorption frequency. We found that narrowing down to the  $|600|$  Oe range, namely the center of the hysteresis, was the best indication of changes in magnetic anisotropy. All processing was done in Igor.

To simplify and speed up the process of plotting and fitting, code was written in Igor, which can be found in the appendix. The code has been annotated for convenience, but will also be discussed here.

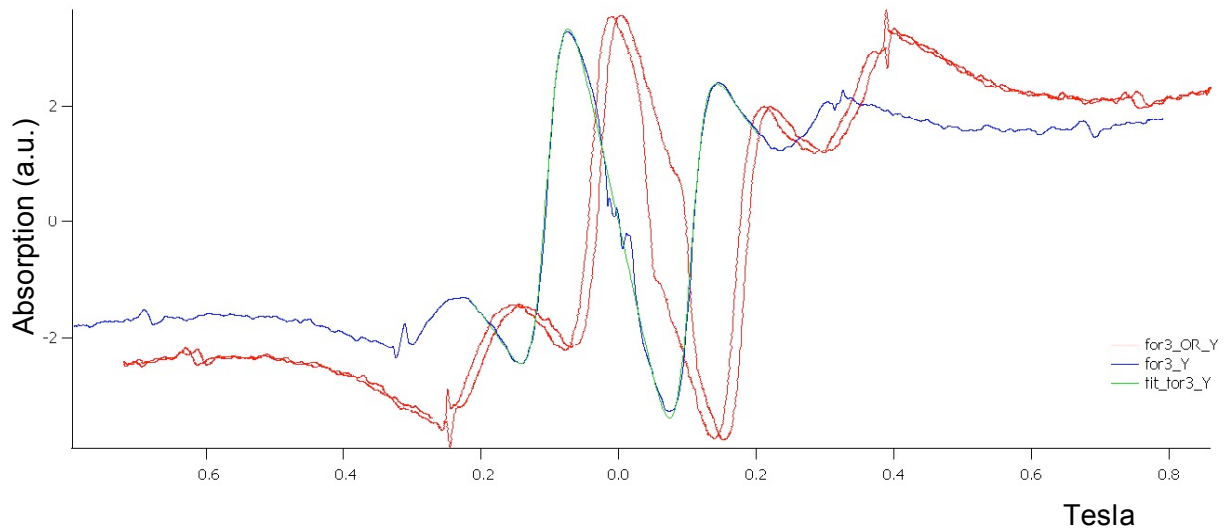


*Figure 20, (Red) Original data, (Blue) processed data, (green) fitted FMR absorption plots.*

Raw data is loaded into Igor, and is first set to the correct data type by using the `loadwve` script with appropriate variables (the red data on figure 20). From this the data is to be normalized using a consistent approach. In this case, the distance between the maximum and minimum y-values of the signal ‘blip’ at around -0.25 T (on figure 20) are set to equal 1. This is done by dividing the y-values of the raw data by the difference between the max and min ‘blip’ y-values. Repeating this for all data sets makes a uniform y-axis data set, compensating for any measurement errors.

Next the wave objects are processed by the `dolt` script. Before this script is called, two graph markers need to be placed on the Igor graph (a function of Igor). These are two known points to be equidistant from the center of the hysteresis. In our case, we again used the ‘blips’, placing the A and B markers on the top peak of the left and right blips of the raw data (red in figure 20), respectively.

This script goes on to do some more data processing, putting everything in the right format so Igor can work with it, and then calls `prepareWave`. There the hysteresis loops are first centered using the A and B variables set by the user. This is to compensate for any magnetic offset during measurements (the magnetometer is not connected to the computer during measurements, and values have to be manually entered). The waves are then smoothed using the Igor `Smooth` command, by a factor of 30.

To remove the hysteresis the raw data is derived and saved as a new wave object, which is also smoothed by a factor of 100. The original wave and the derivation multiplied by a constant (depending on the data set this constant can differ; visual confirmation is needed) are subtracted as shown by the blue graph on figure 20.

The same thing should be done for the background noise data set, which must be subtracted from the blue data set. This properly formatted data can now be fitted to.

The `extractData` fits a Lorentzian to the blue graph, resulting in the green graph on figure 20. The visual overlay is a feature of the code that can be used to confirm proper fitting. The resulting coefficients are presented to the user on the command box. The following equation was used:

$$s = a + b * H + c * \frac{H - H_0}{(H - H_0)^2 + G^2} + c * \frac{H + H_0}{(H + H_0)^2 + G^2}$$

Here,  $s$  = new fitted y-values,  $a$  = y-axis offset,  $b$  = x-axis offset,  $c$  = fitting constant,  $H$  = magnetic field (x-values),  $H_0$  = peak absorption field,  $G$  = fitting parameter. These are the outputs of `extractData`.

### Results and Discussion

After all data sets had been collected, we noticed an interesting phenomenon around the area of maximum absorption, the cross-over of the x-axis. Figure 21 shows the notable area with red circles highlighting them. Note how ‘flat’ this area is.

We took the FMR data from several voltage cycles, plotted them over each other concentrating on this region, and found that this flat feature disappears and reappears, depending on the applied electric field. Figure 22 shows this relation, focusing on the graph plots.

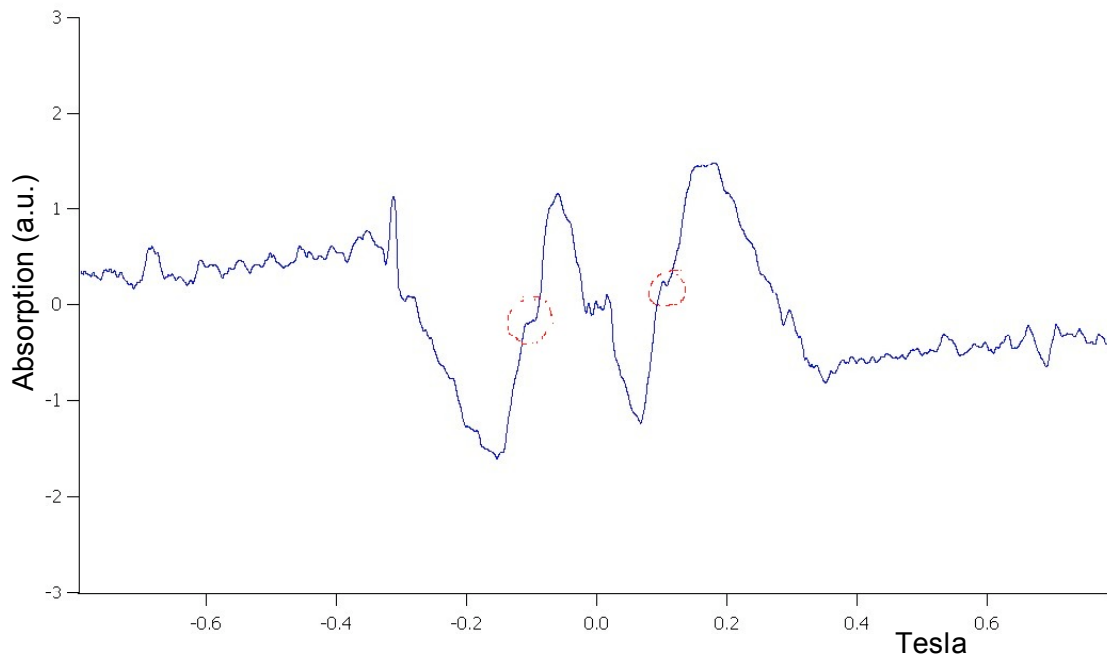


*Figure 21, Formatted FMR data with (red circles) interesting x-axis cross over feature.*

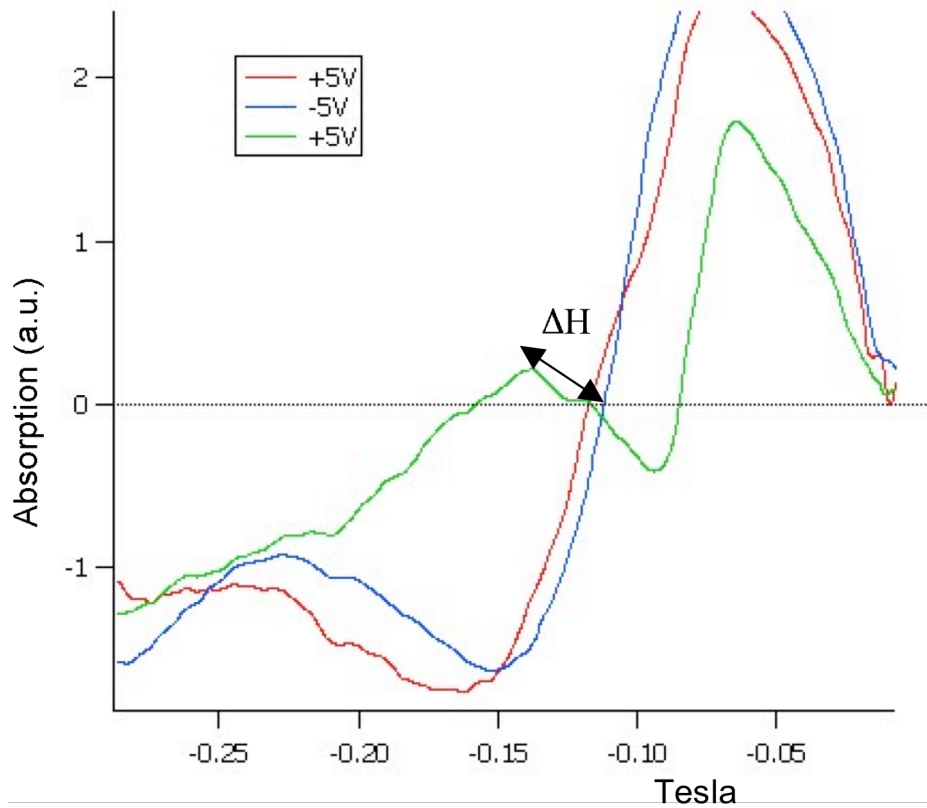


Figure 22, Close-up of the 'flat' region on the FMR data over a +/-/+ voltage cycle..

The flat area was characterized by the magnetic field it spanned ( $\Delta H$ ), meaning that graphs without a flat area had no span ( $\Delta H=0$ ). Plotting these values we find an interesting set of data, shown in figure 23.

Figure 23 can be broken down into three regions:

- The first region, from 0 to 6 (on the x-axis), is an area with almost no activity.
- The second region, from 6 to 9, is an area with many flat regions present.
- The third, and most interesting, region shows switching from one state of magnetic anisotropy to another. It looks like 1/0 memory state switching.

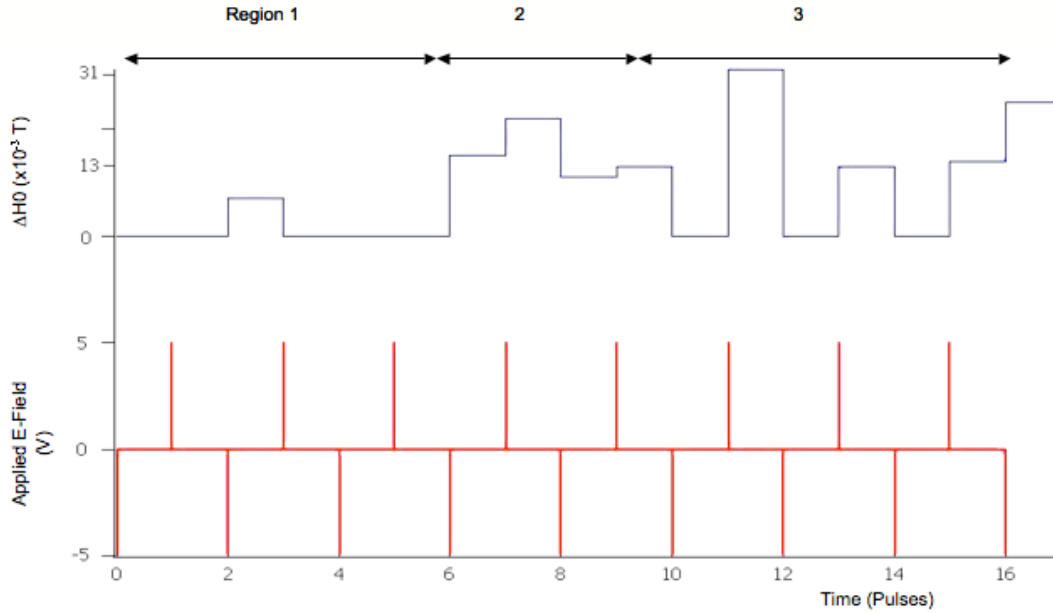


Figure 23, Change in magnetic anisotropy as a function of applied electric field. X-axis values are a representation of the pulse number.

One could imagine the first two regions as being a sort of conditioning run, with proper operation in the third section. However it is worth noting that operation in the third region is not totally uniform. We believe this is due to the size of the FeGa device spanning several PZT grains, causing the in-plane strain effects to cancel or enhance each other. Nevertheless, it is apparent from the data that the converse piezoelectric effect from the PZT bi-layers is indeed transferring the strain, by mechanical transduction, to the FeGa layer. The FeGa layer is thereby undergoing the Villari effect, and changing its magnetic anisotropy.

It was mentioned initially that measurements were taken at 10 degree intervals over a span of 180 degrees. Our findings were that the magnetic hysteresis around the zero crossover did indeed change, becoming larger or smaller, as we moved the easy axis in-plane around the magnetic field. The flat area (as in figure 21), when present, was present

in all these hysteresis loops. For maximum effect, only the angle with the largest hysteresis was used to generate the figures in this section. This chosen angle is consistent amongst all data presented. The actual angle is random, based on initial sample placement.

In going forward, devices must be small enough to minimize opposing effects from the PZT grains, and so ideally be around the 1  $\mu\text{m}$  range. Unfortunately this is too small to use an FMR setup to probe the magnetic anisotropy. Therefore other methods must be applied. We went on to do anisotropic magnetoresistance measurements, discussed in the following section.

## **AMR**

Anisotropic magnetoresistance measurements display the resistance of our device with respect to its in-plane orientation in a magnetic field. A four-probe device was designed for this purpose, as discussed in chapter 2 and illustrated in figure 15. A Keithley Sourcemeter was used to apply the current to the top and bottom electrode, and another Keithly Sourcemeter used to measure the voltage between the two center electrodes. This device was wire-bonded to a non-magnetic chipcarrier, and placed within the tube in a custom sample holder. The sample holder is a piece of clear PVC tubing, about an inch in diameter, held up by two strips of aluminium with holes cut in them to let the tube through. The setup was clamped down onto an aluminium table. Figure 24 is a photo of our experimental setup, with an exploded view of the sample in its holder (inset).

Wirebonding, and sample placement, proved to be very precarious.

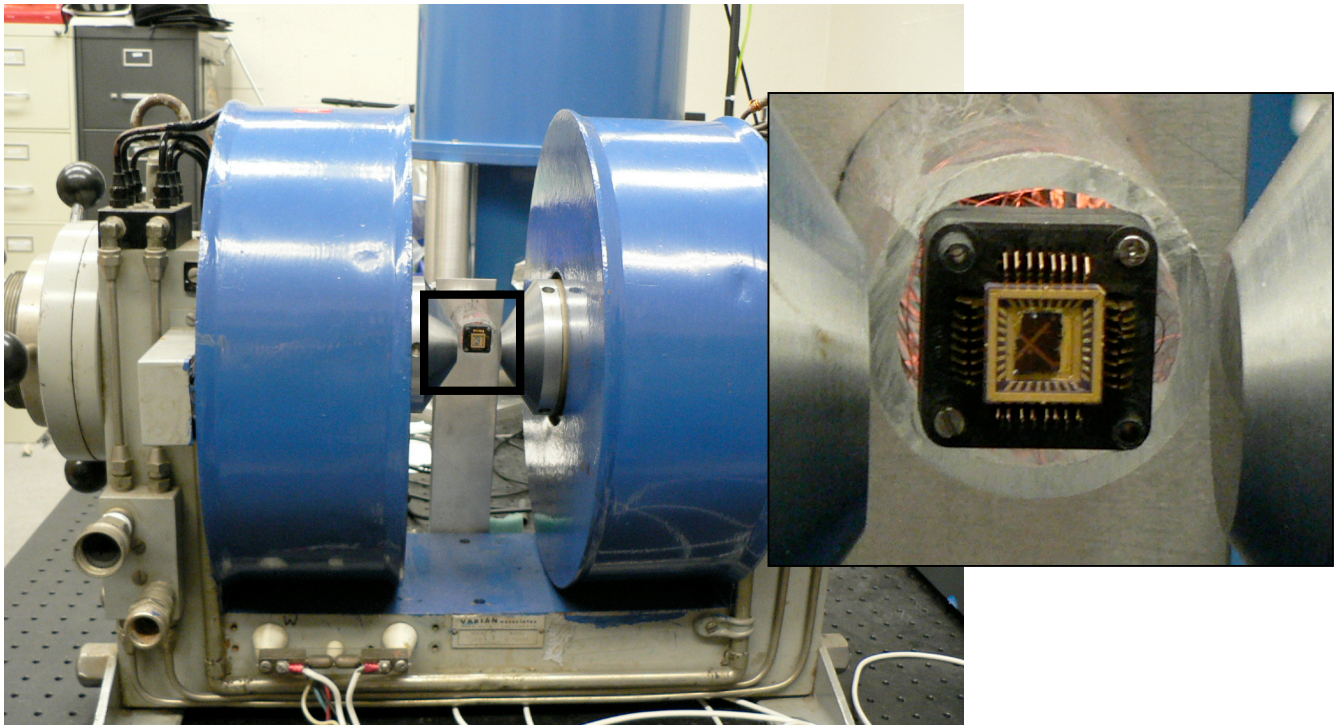


*Figure 24, Our AMR setup with (inset) close-up of the device in its chip carrier.*

The first step was to find a current at which to measure the magnetoresistance. Too much current and the small gold electrodes would simply blow up. Too little, and the resistance readings would get lost in noise. We found that 1 mA ( $3 \times 10^7 \text{ A/m}^2$ ) was appropriate to get good readings, but as high as 3 mA ( $1 \times 10^7 \text{ A/m}^2$ ) would still work (and get better readings, though at reduced life-span).

Figure 25 shows the results of several biasing schemes. The ‘no bias’ (as in virgin state) device shows an AMR value of 0.24%. We can see anisotropic magnetoresistance, as there is a clear difference between resistance when the magnetic field is parallel or perpendicular to the applied current. However, it is not apparent from this data that there is any actual switching as a direct result of the applied electric field.

We believe that this is due to complications involved with the device fabrication, such as leaky PZT. As we are indeed seeing the expected sinusoidal anisotropic magnetoresistance signal, it seems the top electrodes are working as expected and convey the four-probe resistance. More likely the issue lies with an resistive connection of a top probe to the bottom electrode, due to leaky PZT.

Despite this, we believe AMR to be a valid method, and indeed a valid goal, in proving the operation of this device. There is more work to be done on this method, but a basis has been set up: the device fabrication and operation parameters have been determined, and along with the FMR data show much promise for these devices.

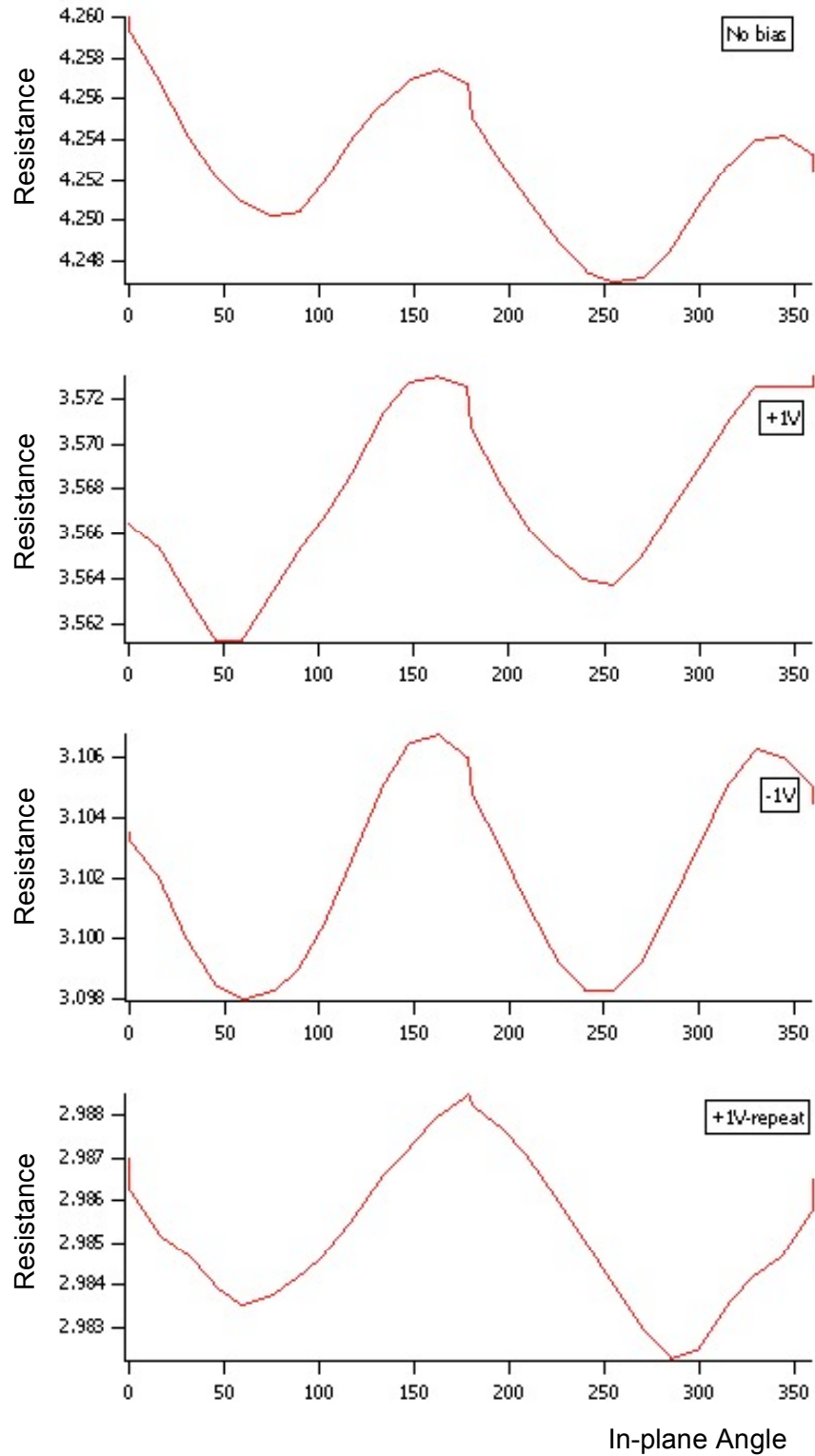


Figure 25, AMR measurements of the transport device under several bias schemes applied in order of top to bottom. Resistance on the y-axis, and in-plane rotation on the x-axis.

## Chapter 5

### Future Work and Conclusions

#### Kerr Microscopy

A Kerr microscope displays the change in light reflection off a magnetic surface. This is due to the magneto-optic Kerr effect, where light reflected off a magnetic medium has a different polarization. [27]

A source of light (white Hg source in our case) is polarized and shines on the surface of the material, which is placed within an oscillating magnetic field. This light is reflected off the sample into the optics, and is projected onto a CCD chip after going through an analyzer. The derivative of the image is then displayed on a computer, to show how the intensity of the polarized light changes with the magnetic field sweeps. Figure 26 illustrates a typical setup.

Figure 27 shows an example of what a 100 nm FeGa film grown on Si looks like under this microscope. Note the presence of the light and dark spots, which show magnetic domains of differing polarizations. This is illustrated by the arrows on the image.

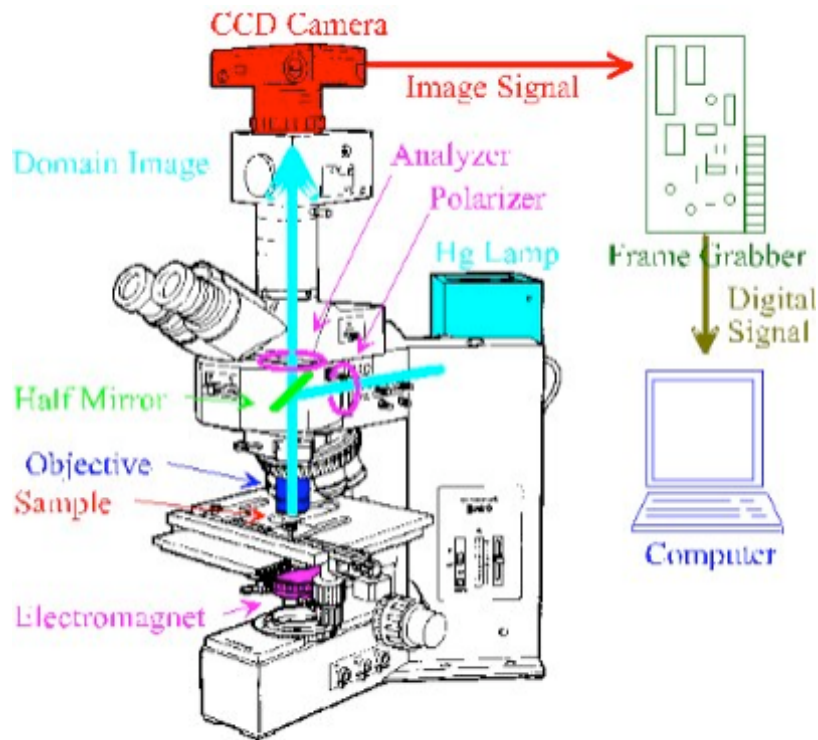


Figure 26, Schematic of Kerr microscope (Source: 25)

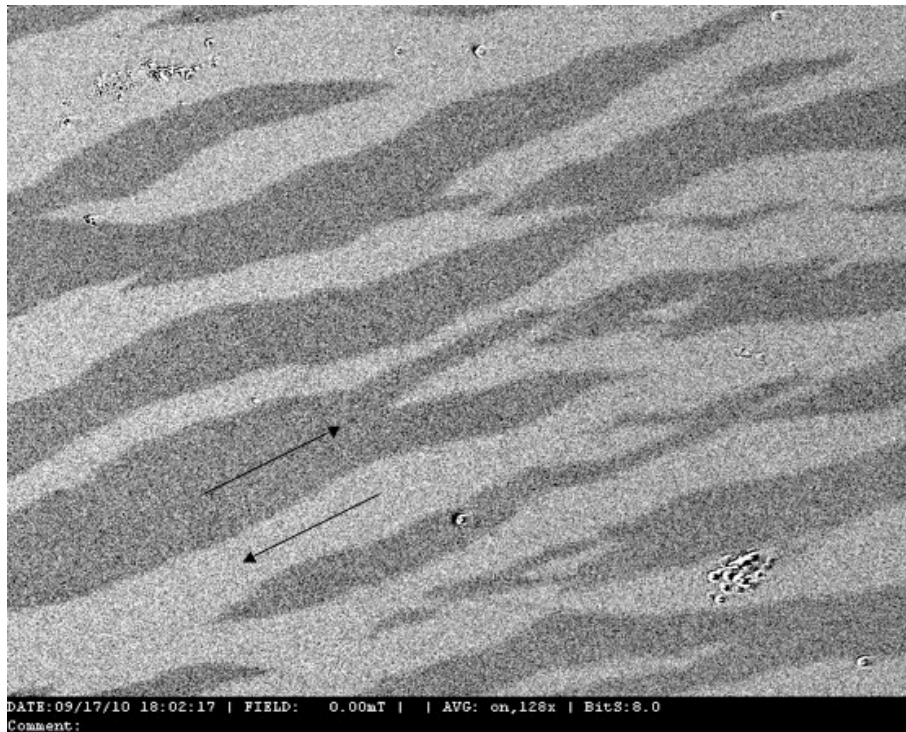
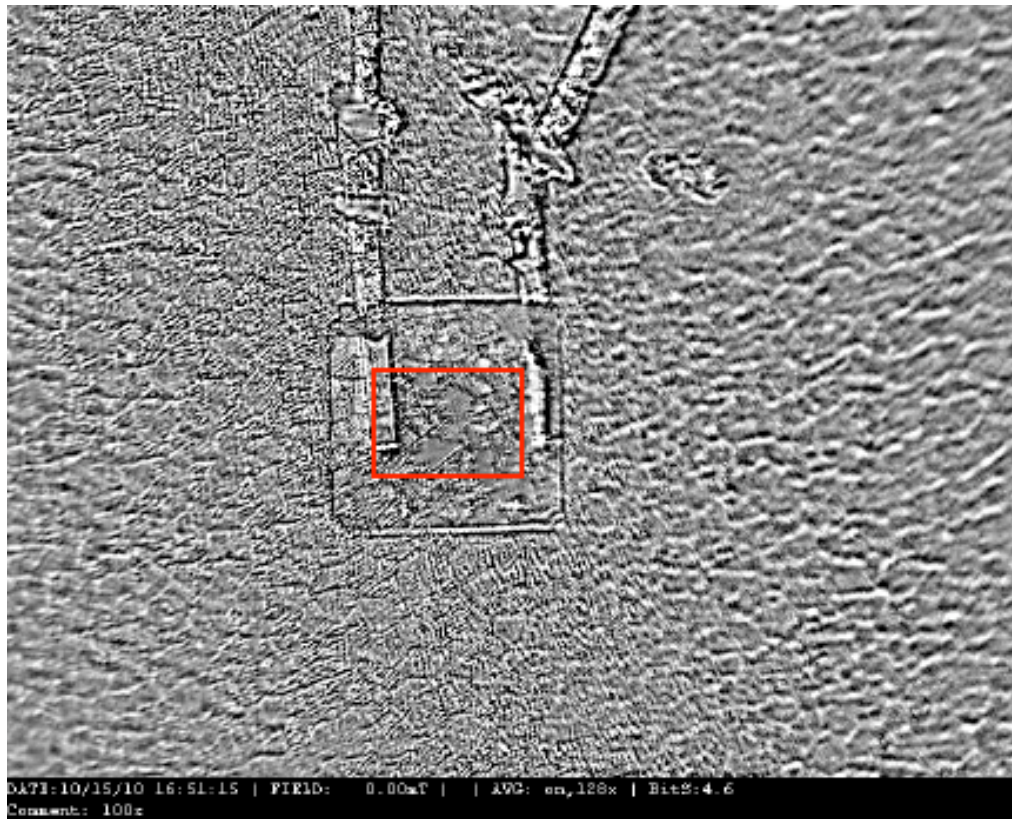


Figure 27, Image from a Kerr optical microscope showing magnetic domains on a 100nm FeGa thin film grown on Si, taken at 50x.

It is not unreasonable to assume that our device would show similar patterns on its surface. Figure 28 shows one of our devices under a Kerr microscope. The red box in the center shows a darker region: a magnetic domain with different polarization than the surrounding regions. Video footage shows the domain growing and shrinking. A gold contact lead (and another one for redundancy) on the surface is used to apply an electric field to the device. In doing so we expect to see the magnetic domain change shape, either by contracting or expanding, and can even take a video of it doing so.



*Figure 28, Kerr microscope image of a 50x50  $\mu\text{m}$  FeGa/PZT device with a magnetic domain boxed in red, taken at 100x.*

Unfortunately, the reality is that this technique has technical limitations. For one, the device has to be rather large. The image above is of a 50x50  $\mu\text{m}$  device, which spans several PZT grains. This may lead to a reduced strain transduction, and so a smaller

Villari effect. Another disadvantage is that at these magnifications the optical lens needs to touch the surface of the material. This means that an optical oil needs to be used, which, although non-conducting, could have an impact on the way the electric field is applied. The most pressing concern is that the image quality from a Kerr microscope is heavily influenced by the roughness of devices; something the two electrodes on the surface heavily impact. Our PZT films are also quite rough, which is still visible through the thin FeGa layer.

With further investigation it should be possible to modify our device sufficiently so it can be analyzed using a Kerr microscope. A single wavelength light source, as apposed to the white light Hg source, would also improve resolution. The most appealing aspect of this is the possibility of having video footage of a device switching from state '0' to '1', repeatedly.

## SEMPA

*SEMPA measurements were carried out at NIST, Gaithersburg MD 20899, in collaboration with John Unguris*

Scanning electron microscope with polarization analysis, or SEMPA, is similar to a Kerr microscope, except that instead of being an optical process, here the SEM's secondary electrons emitted from the surface are spin polarized. They are analyzed using specific detectors, such as a Mott detector. The advantage is that an SEM is capable of reaching much higher orders of magnification, and can also take videos. [28]

Recently it was found using SEMPA that a similar device to ours, with permalloy rather than FeGa as the magnetostrictive material, showed what we believe to be vertical magnetic domains (Figure 29). With the same device used in Kerr (namely with two gold electrodes) it should be possible to show how these magnetic domains move. This is currently under investigation.

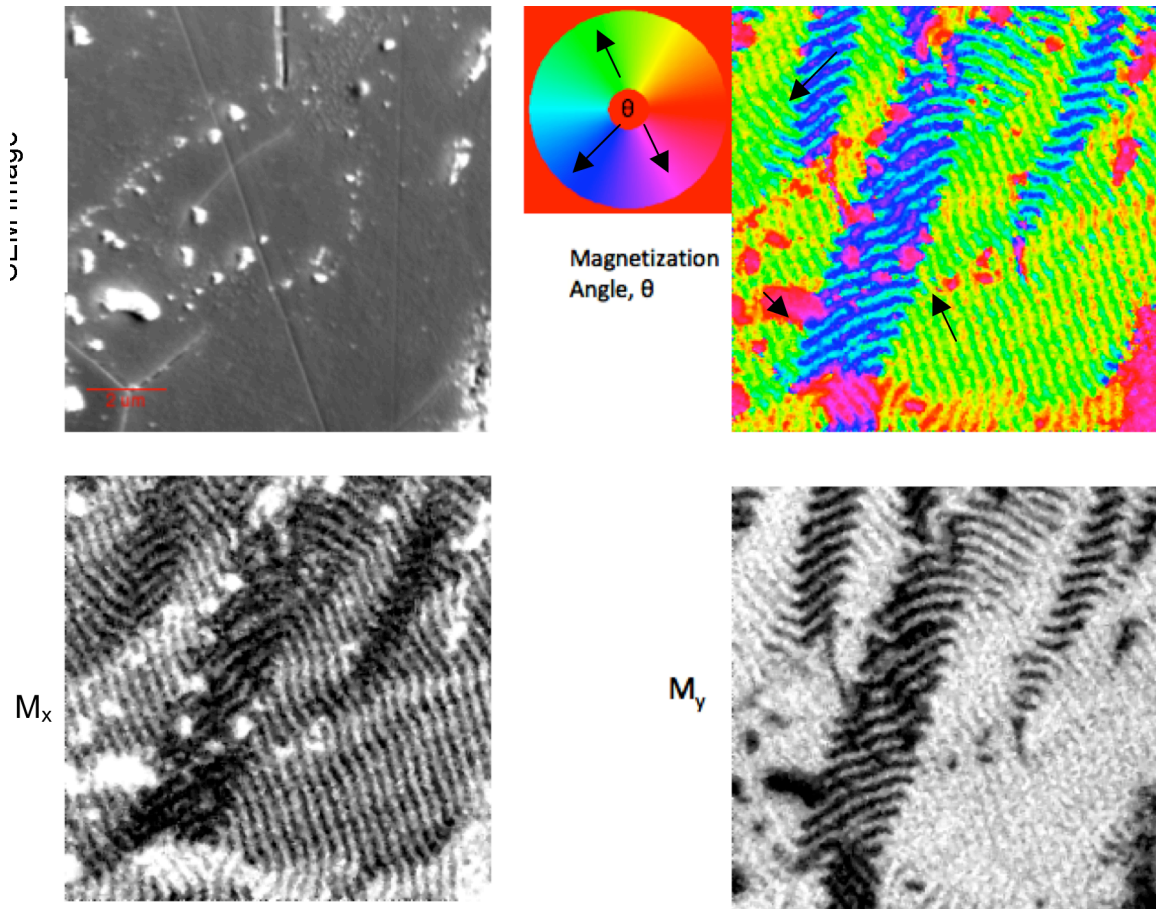


*Figure 29, Sempa images showing (clockwise from top left) film morphology, magnetization plot (with color disk showing magnetic field direction), vertically applied magnetic field, horizontally applied magnetic field. Note vertical magnetic domains.*

Based on the preliminary SEMPA results, magnetic force microscopy (MFM) images of the permalloy device were taken, showing vertical magnetic domain walls. After applying an electric field, domain wall motion was noted (figure 30). It seems the vertical

magnetic domain walls are the result of induced stress from the PZT bi-layers, as they are not present on a device with a single PZT layer.

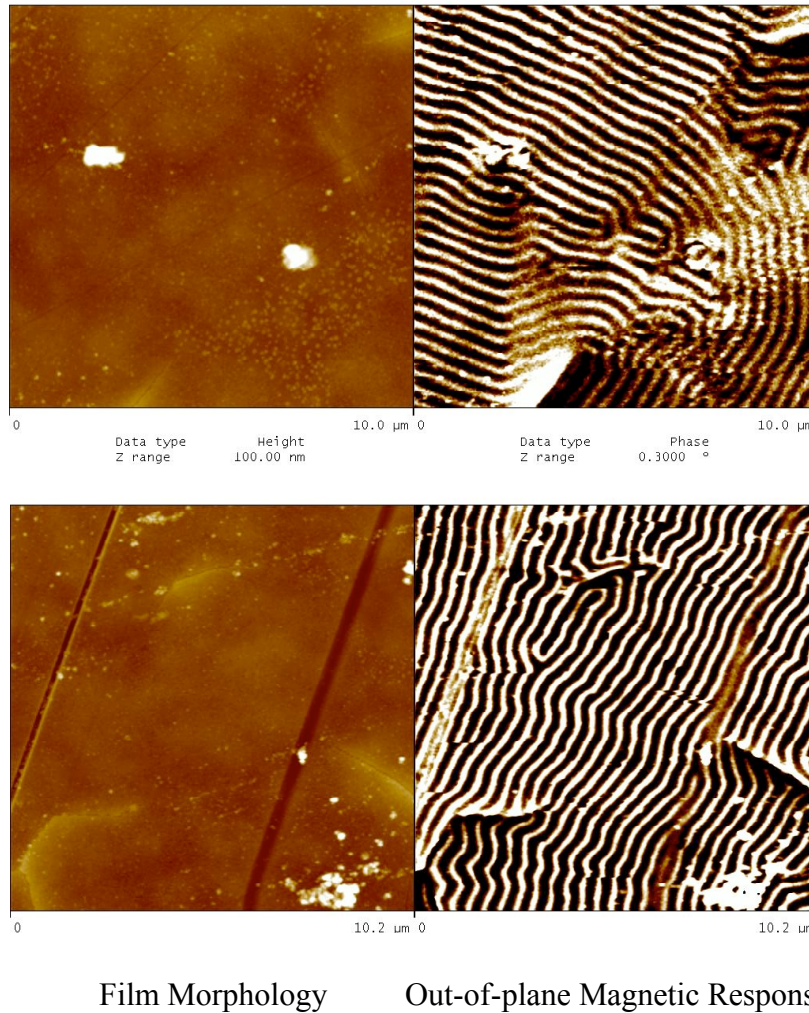


*Figure 30, MFM images (Top) as grown and (bottom) +7V applied for 30 seconds permalloy film on PZT bilayers, showing out-of-plane magnetic state change.*

## Conclusion

In this thesis we have demonstrated the feasibility of combining a thin film of FeGa, a magnetostrictive material, and PZT thin films, a piezoelectric material with reversible twin boundary motion, to make a spintronic converse magneto-electrically coupled device. These materials are all thin films, are low power consuming, and operate at room

temperature. Details on the fabrication of a FMR and an AMR device are presented: growth parameters and fabrication tools. Measurement details and device operating conditions are presented. We have shown, by means of probing the magnetic anisotropy by FMR, that it is possible to apply an electric field to the heterostructure, straining the PZT, thereby changing the magnetic anisotropy of the mechanically coupled FeGa magnetostrictive layer. We have demonstrated that the PZT bi-layers, despite being thin films grown on a substrate, exhibit the ability to overcome the substrate clamping effect. We have demonstrated that once a strain induced magnetic anisotropy state is achieved in the FeGa film, it is retained until an electric field is applied. This is due to the domain wall motion in the top ferroelastic PZT layer that only happens when an electric field is applied. We have demonstrated that further investigation is necessary to study the effects of PZT on magnetostrictive films in inducing vertical magnetic domains.

More generally, we have demonstrated that heterostructures such as ours, as a combination of the intrinsic properties of two distinct materials, show potential towards future magneto-electrical coupled devices. A combination such as ours works under much more tolerable conditions, as opposed to single materials exhibiting both properties: low field and room temperature operation, with significant results. This is due to the specific choice of materials for the magnetostrictive and piezoelectric effect. Through further investigation, such as AMR, Kerr, and SEMPA measurements, converse magneto-electric devices combining the intrinsic properties of two different materials will prove to be a potentially effective approach towards MRAM chips, sensors, and more.

## Appendix

Igor FMR processing code:

### **processAndFit.ipf**

---

```
#pragma rtGlobals=1          // Use modern global access method.

//For fitting FMR signals to get Lorentzian fitting parameters

//*****

// OPERATING INSTRUCTIONS:

//

// 1. Load the file in Igor, name as *_OR_X, *_OR_Y

// 2. loadwve("waveX","waveY",waveORX,waveORY")

    (string,string,wave,wave)

// 3. Do any normalisations after this on both _Y **AND** _OR_Y (for the blips)

// 4. Find points A and B          (to centre the graph)

// 5. doIt(waveX,waveY,waveORX,waveORY)

    (wave,wave,wave,wave)

// 6. Adjust the y-axis

// 7. ModifyGraph rgb(waveY)=(0,0,65280)          (optional, to change the
colour of the new graph)

//

// After all this you will have the original graph plus the new, centered graph,
```

without hysteresis loops

```
// 8. Remove background noise
```

```
// 9. Fit graph. Equation used:
```

```
//FMR2:  $f(H) = a + b \cdot H + c \cdot \frac{(H - H_0)}{(H - H_0)^2 + G^2} + c \cdot \frac{(H + H_0)}{(H + H_0)^2 + G^2} + c_2 \cdot \frac{(H - H_{02})}{(H - H_{02})^2 + G_2^2} + c_2 \cdot \frac{(H + H_{02})}{(H + H_{02})^2 + G_2^2}$ 
```

```
// To remove data after a fit, do 'extract data':
```

```
// extractData(number) (integer)- number signifies wave number.
```

```
//Requires waves : a b c H0 G, preferably all in a table.
```

```
//Additional:
```

```
//extractData2(number)
```

```
//Same as above but has a second set of lorentzians (c2, H02, G2)
```

```
//*****
```

```
function loadwve(waveX, waveY, waveORX, waveORY)
```

```
wave waveORX, waveORY
```

```
string waveX, waveY
```

```
Duplicate /o waveORX $waveX
Duplicate /o waveORY $waveY
Display /W=(0,0,1000,420) waveORY vs waveORX
Legend/C/N=text0/F=0/A=MC
ShowInfo

end function
```

```
function dolt(waveX,waveY,waveORX,waveORY)
// Called from main(). Takes the global wave variables (strings and wave
objects), sets them to the correct variables, sends it to 'prepareWave' for
centering and formatting, finally plots the graphs. Returns to main().
```

```
wave waveX,waveY,waveORX,waveORY
waveX=waveORX;
waveY=waveORY
prepareWave(waveX,waveY,23,waveX(pcsr(B)),waveX(pcsr(A)));
AppendToGraph waveY vs waveX;

end function
```

```

function prepareWave(xWave,yWave,cst,left,right)
//Called from dolt(). Centers the plot, smoothes the x-axis, Removes the
hysteresis loop, should return to dolt()
wave xWave,yWave;
variable cst;
variable left,right;
//wave outX = xWave;

xWave--=(right-left)/2+left;           //Centre graph

Smooth 30, xWave;DelayUpdate;          //Smooth the x-axis to get
rid of the irratic behaviour

Differentiate xWave/D=xWave_DIF;DelayUpdate; //Derive
Smooth 100, xWave_DIF;DelayUpdate;

xWave--=xWave_DIF*cst;                 //Get rid of the hysteresis
loop where not necessary

Sort xWave yWave,xWave; DelayUpdate
Smooth 100, yWave;

```

```
end function
```

```
function extractData2(number)
```

```
variable number;
```

```
wave '2a','2b','2c','2H0','2G','2c2','2H02','2G2';
```

```
wave W_coef
```

```
'2a'[number]=W_coef(0);
```

```
'2b'[number]=W_coef(1);
```

```
'2c'[number]=W_coef(2);
```

```
'2H0'[number]=W_coef(3);
```

```
'2G'[number]=W_coef(4);
```

```
'2c2'[number]=W_coef(5);
```

```
'2H02'[number]=W_coef(6);
```

```
'2G2'[number]=W_coef(7);
```

```
end function
```

---

## REFERENCES

1. Lee, Moon, Park, et al, Proceedings of the 2008 ACM SIGMOD intl. conference on Management of data, New York, NY, 1075-1086 (2008)
2. Binek, Doudin, J. Phys.: Condens. Matter **17** (2005) L39–L44
3. Nan, Bichurian, Dong, et al, JAP **103**, 031101 (2008)
4. Chu, Martin, Holcomb, et al, Nature **7**, 478-482 (2008)
5. Wang, Liu, Ren, Adv. Phys. **58**, 321 (2009)
6. Zhao, Zhao, Hunter, et al, APL **94** 243507 (2009)
7. Overby, Chernyshov, Rokhinson, arXiv:0801.4191v1 (2008)
8. T. Kimura et al, Nature **426** (2003), 55
9. Shirane, Sawaguchi, Takagi, Phys. Rev. **84** (3), 1951
10. Q. Zhou, E. Hong, et al, Mat. Res. Soc. Symp. **655**, CC11.7.1
11. V. Nagarajan, I. Jenkins, et al, J. Appl. Phys. **86** (1), 1999, 595-602
12. M. Adachi, T. Matsuzaki, Japanese J. Appl. Phys., **26** (4), 1987, 550
13. “PZT”, Department of Materials Science and Metallurgy, University of Cambridge, <<http://www.doitpoms.ac.uk/tlplib/piezoelectrics/pzt.php>>
14. F. C. Kartawidjaja, C. H. Sim, J. Wang, J. Appl. Phys. 2007, 102, 124102
15. A. Varatharajan, D. Kan, et al, Adv. Mater. **2009** (21), 3497-3502
16. Ganule, Nagarajan, Hill, et al, J. Appl. Phys. **2002**, 91, 1477
17. Hattrick-Simpers et al, APL **93**, 102507 (2008)
18. “Discovery of giant magnetoresistance in annealed  $\text{Co}_{1-x}\text{Fe}_x$  thin films”, D. Hunter et al, in preparation.

19. Pettiford, J. Lou, L. Russel, et al, APL **92** 122506 (2008)
20. Zhao, Lord, APL **99**, 08M703 (2006)
21. Kittel, Phys. Rev. **73** (2) (1948)
22. “Broadband Ferromagnetic Resonance System”, Patton Group, Colorado State University,  
<[http://www.physics.colostate.edu/groups/PattonGroup/systems/bbfmr\\_desc.html](http://www.physics.colostate.edu/groups/PattonGroup/systems/bbfmr_desc.html)>  
>
23. Tondra, Lottis, Riggs, J. Appl. Phys. **73** (10) (1993)
24. “Introduction to solid state physics” (8<sup>th</sup> edition), Kittel, John Wiley and Sons (2005)
25. “Experimental Facilities”, Center for Nanospinics of Spintronic Materials, Korea Advanced Institute of Science and Technology,  
<<http://cnsm.kaist.ac.kr/facility.htm>>
26. Electrical Properties of Materials (8<sup>th</sup> edition), Solymar and Walsch, Oxford University Press (2010)
27. C. Mudivarthi, S. Na, et al, JMMM **322** (14), 2010, 2023-2026
28. M. Scheinfein, J. Unguris, et al, Rev. of Sci. Instr., **61** (10), 1990, 2501-2527